Experimental and Molecular Pathology 90 (2011) 91–96

Contents lists available at ScienceDirect

Experimental and Molecular Pathology

journal homepage: www.elsevier.com/locate/yexmp

MT1-MMP plays an important role in an invasive activity of malignant pleural mesothelioma cell☆

Takefumi Doi [a], Yoshimasa Maniwa [a,*], Yugo Tanaka [a], Shinya Tane [a], Shotaro Hashimoto [a], Yoshiharu Ohno [b], Wataru Nishio [a], Yoshihiro Nishimura [c], Chiho Ohbayashi [d], Yutaka Okita [e], Yoshitake Hayashi [f], Masahiro Yoshimura [a]

[a] Division of Thoracic Surgery, Kobe University Graduate School of Medicine, Kobe, Japan
[b] Department of Radiology, Kobe University Graduate School of Medicine, Kobe, Japan
[c] Division of Respiratory Medicine, Kobe University Graduate School of Medicine, Kobe, Japan
[d] Division of pathological oncology, Kobe University Graduate School of Medicine, Kobe, Japan
[e] Division of Cardio-vascular Surgery, Kobe University Graduate School of Medicine, Kobe, Japan
[f] Division of Molecular Medicine and Medical Genetics, Kobe University Graduate School of Medicine, Kobe, Japan

ARTICLE INFO

Article history:
Received 6 June 2010
Available online 19 October 2010

Keywords:
Malignant pleural mesothelioma
Invasion
MT1-MMP
RNA interference
Double-layered collagen gel hemisphere

ABSTRACT

Malignant pleural mesothelioma (MPM) has a poor prognosis and is a treatment resistant tumor, which is increasing in frequency throughout the world. The poor prognosis is due to the aggressive local invasiveness rather than distant metastasis. In this study, we established a cell line of malignant mesothelioma from a clinical specimen and assessed the relationship between the expression of MT1-MMP and the invasion ability of that line, as well as the cultured cells of several other lines, using the simple method that we created previously. We established a cell line from a clinical specimen from a patient with malignant mesothelioma. We assessed the invasive activities of MPM cells in an easy-to-prepare double-layered collagen gel hemisphere (DL-CGH) system that enabled us to visualize cell movements during invasion. To assess the role of MT1-MMP in the invasive activity of MPM cells, we knocked down its expression by RNA interference (RNAi). The invasion assay with DL-CGH revealed that a high expression of MT1-MMP in MPM cells was associated with aggressive invasive activity. The RNAi of MT1-MMP indicated that the expression of MT1-MMP might have a crucial role in the invasiveness of MPM cells. The MT1-MMP expression in MPM cells is related to their capacity for locally aggressive spreading into the pleura and the surrounding tissues, and MT1-MMP should be a suitable molecular target for the suppression of the invasiveness of MPM.

Introduction

Malignant pleural mesothelioma (MPM) has a poor prognosis and is a treatment resistant tumor, which is increasing in frequency throughout the world (Robinson et al., 2005). MPM is not likely to metastasize distantly to other organs; its malignancy is due to its locally aggressive spreading into the pleura and surrounding tissues (Zhong et al., 2006; Pistolesi and Rusthoven, 2004).

It is said that the microenvironment (both cellular and extracellular elements) of the local host tissue plays an important role in the process of tumor cell invasion and that interaction between the ECM and tumor cells is essential for the degradation of ECM by the tumor cells (Liotta and Kohn, 2001). Matrix metalloproteinases (MMPs) are proteins that play an important role in this process (Curran and Murray, 2000).

The MMP family consists of more than 25 structurally related, zinc-dependent endopeptidases that are capable of degrading the basement membrane and the ECM (Konstantinopoulos et al., 2008). Among the members of this family, MMP-2 and MMP-14 play important roles in the MPM, and some epithelial malignant tumors show the overexpression of MMP-14 (Atkinson et al., 2007; Edwards et al., 2003). MMP-14, which is known as a membrane-type matrix metalloproteinase (MT-MMP), is mainly concentrated at the surface of the cells (Sato et al., 1994; Takino et al., 2007), so it is possible that MT1-MMP directly contributes to the degradation of the ECM. Because of these characteristics we focused on MMP-14 (MT1-MMP) as one of the potentially important factors that help MPM spread directly into other organs. Moreover, various methods for *in vitro* 3-D studies of cell invasion using a collagen gel have been described (Albini et al., 1987; Nyström et al., 2005; Duong et al., 2005; Takata et al., 2007), and we believe that these methods are very useful for the assessment of the invasion ability of MPM.

☆ Sources of support: Grant 18591547 from the Japan Society for the Promotion of Science (to Y.M.).

* Corresponding author. Division of Thoracic Surgery, Kobe University Graduate School of Medicine, Mailing address: 7-5-2, Kusunoki-cho, Chuo-ku, Kobe, Japan, 650-0017. Fax: +81 78 382 5959.
E-mail address: maniwa@med.kobe-u.ac.jp (Y. Maniwa).

0014-4800/$ – see front matter © 2010 Elsevier Inc. All rights reserved.
doi:10.1016/j.yexmp.2010.10.008

In this study, we established a cell line of malignant mesothelioma from a clinical specimen. We then assessed the relationship between the expression of MT1-MMP and the invasion ability of this established cell line and other cell lines using the simple method that we created previously (Takata et al., 2007).

Materials and methods

Cell lines

The A549 (bronchiolo-alveolar carcinoma of lung) cell line was obtained from the Health Science Research Resources Bank (Osaka, Japan); the WI-38 cell line was obtained from the RIKEN Bioresource Center (Tsukuba, Japan). NCI-H28 (pleural effusion), NCI-H2452 (epithelial mesothelioma) and MSTO-211H (biphasic mesothelioma) were obtained from the American Type Culture Collection (Manassas, USA). Cells were maintained in RPMI-1640 medium supplemented with penicillin (100 U/mL), streptomycin (100 U/mL), and 10% bovine calf serum.

Establishment of a cell line of malignant mesothelioma

A clinical specimen from a patient with malignant mesothelioma was minced finely using scalpel or razor blade and digested in a cell dispersion enzyme solution (EZ; Nitta Gelatin Inc., Osaka, Japan) for 2 h. The dispersed cancer cells were treated with ethylene-glycol-tetra-acetic acid (EGTA)-trypsin and filtered through a 200-μm nylon mesh. The cells were then incubated in a collagen-gel-coated flask (CG-flask; Nitta Gelatin Inc., Osaka, Japan) containing a preculture medium with 10% fetal bovine serum (FBS; PCM-1; Nitta Gelatin Inc., Osaka, Japan) at 37 °C in 5% CO_2 overnight. We collected the viable cancer cells that adhered to the collagen gel and performed repeated subculturing until fibroblasts and other normal cells had disappeared.

Immunohistochemistry

Immunohistochemistry was performed to detect the MT1-MMP expression in paraffin sections, and tissue microarray samples were analyzed immunohistochemically. The MT1-MMP primary antibody (MAB3328, Chemicon International a Serologicals Company) was diluted 1:100 in a blocking solution before use. This diluted primary antibody was added to the tissue sections and incubated overnight at 4 °C. Antigen–antibody complexes were detected by the avidin–biotin peroxidase method (Vectastain Elite ABC Kit, Vector Laboratories, Inc., Burlingame, CA) and diaminobenzidine tetrahydrochloride reagents (DAKO EnVision™/HRP, Dako, Japan). Sections were counterstained with hematoxylin.

Western blotting

Cultured cells washed with PBS^- were lysed with 100-μl Laemmli sample buffer, and 10 μl of these samples were analyzed by SDS-PAGE. Then, the separated bands were transferred to nitrocellulose membranes (Amersham Biosciences Corp.). After washing the membranes with PBS-T, they were blocked for 30 minutes (5% skim milk, diluted by PBS-T). Following 2 rinses with PBS-T, membranes were incubated (1 hour, room temperature) with the primary antibody for MT1-MMP (MAB3328, Chemicon International a Serologicals Company), which was diluted 1:500 with 5% BSA/PBS-T. After washing with PBS-T, membranes were incubated (30 minutes, room temperature) with the secondary peroxidase-labeled sheep anti-mouse Ig whole antibody (Amersham Biosciences Corp.), which was diluted 1:5000 with PBS-T. Membranes were then washed with PBS-T and visualized using the luminoimage analyzer LAS-3000(Fuji film Inc., Tokyo, Japan) treated with a detection kit (Amersham Biosciences Corp.).

As a control assay, we performed Western blotting using the same membranes. The primary antibody was directed against β-actin (#AB6276, Abcam, Cambridge, UK), and the secondary antibody was peroxidase-labeled sheep anti-mouse Ig whole antibody (Amersham Biosciences Corp.).

Preparation of double-layered collagen gel hemispheres

Acid-soluble collagen I (Nitta Gelatin Inc., Osaka, Japan), tenfold concentrated Ham's F-12 medium, and reconstruction buffer (2.2-g $NaHCO_3$ + 4.77-g HEPES in 100 ml of 0.05-N NaOH) were mixed at a volume ratio of 8:1:1 and then seeded with cultured cells at a density of 3.0×10^6 cells/ml. Five microliters of the mixture, containing 3.0×10^4 cells, were dropped onto a plastic dish. Once the mixture had gelled, a second 30-μl drop of collagen was placed exactly on the top of the first gel drop, encapsulating it completely. The gel hemisphere was then submerged in medium and cultured. Cells were then stained with neutral red, and the gel was allowed to dry. The invasive activity of the cells was evaluated by measuring the expansion of red stain into the outer collagen layer.

RNA interference (RNAi) in WI38 and established mesothelioma cells

RNAi was performed with commercially available siRNAs (HP-validated siRNA for MT1-MMP; Qiagen GmbH, Hilden, Germany) and a non-silencing control siRNA (target sequence; AAT TCT CCG AAC GTG TCA CGT, Qiagen GmbH) according to the manufacturer's instructions. Briefly, 24 μl of transfection reagent (Hiperfect; Qiagen GmbH) was suspended in 200 μl of serum-free culture medium containing 6 μg siRNA. After a 10-minute incubation at room temperature, the mixture was added to WI38 and established mesothelioma cell culture (60-mm-round dish with 4-ml culture medium containing 10% fetal bovine serum and antibiotics mentioned above) grown to 60% confluence; the final concentration of the siRNA was 100 nM. After 24 hours (at 37 °C, 5% CO_2), these cells were suspended in phosphate buffered saline (PBS) and the cell density was calculated to prepare for the encapsulation of the cells in DL-CGH.

Time-lapse motion picture

A Moticam 2000 digital microscopy system (Shimadzu Rika Corp., Tokyo, Japan) was used to create motion pictures of cell invasion. The camera head was set at the position of the eyepiece on an inverted microscope (CKX31; Olympus Corp., Tokyo, Japan), and the entire microscope was then installed in a 37 °C, 5% CO_2 incubator without humidity (to prevent dew formation in the instruments). A DL-CGH prepared in the well of an ordinary 6-well plastic culture plate was submerged in proper medium; the residual 5 wells were filled with water to maintain humidity inside the plate. Cells were observed microscopically using a 10× objective lens, and the camera was operated from a personal computer running the Moticam 2000 software to capture and display images of living cells. Recording initiated 24 hours after DL-CGH culture continued for 96 hours. Images were captured automatically every 20 minutes, with 288 consecutive images stored as 800×600 pixel JPEG files. Using the Windows Movie Maker software (Microsoft Corp., Redmond, WA), we created a 30-second movie (saved as a WMV file) that displayed 288 consecutive images for 0.125 seconds each.

Result

Establishment of a cell line of malignant pleural mesothelioma from clinical specimen

We established an MPM cell line from a clinical specimen. To prove that these cells indeed were MPM, we sent samples of them to the

department of pathology in our hospital and requested an immunohistochemical analysis with calretinin, D2-40, CAM5.2, and AE1/AE3, which are useful markers of MPM (Mimura et al., 2007). While D2-40 was not identified, calretinin, AE1/AE3 and CAM5.2 were stained (Fig. 1). Thus, these cells were proved to be MPM immunochemically, and we had obtained a primary culture of MPM cells.

Expression of MT1-MMP in a clinical sample of MPM

To establish whether MT1-MMP was expressed in the MPM specimen we performed immunohistochemistry on the clinical samples of the MPM patient, following the technique described in Materials and methods (Fig. 2). We show the difference between normal cell structures and tumor cells in Fig. 2a. MT1-MMP was strongly expressed in the tumor cells, especially at the edge of the cells (Fig. 2b). In contrast, MT1-MMP was not expressed in the normal vascular endothelial cells.

Relationship between the MT1-MMP expression and the ability to invade, using cancer cells and normal fibroblasts

Western blotting was performed to determine if MT1-MMP was expressed in the cell lines of lung adenocarcinoma, fibroblasts and MPM (among them, the MPM cell line established in our laboratory). We detected a strong expression of MT1-MMP in WI38 and the established MPM cell line. But the expression of MT1-MMP was very weak in A549, the cell line of lung adenocarcinoma and NCI-H28, one of the acquired MPM cell lines. In the other MPM cell lines (NCI-H2452 and MSTO-211H), the expression of MT1-MMP was moderate (Fig. 3).

Then, we performed invasion assays with these cell lines using DL-CGH. A549 and NCI-H28, which showed a weak expression of MT1-MMP, showed only a minimal tendency to invade into the outer layer of collagen gel, whereas the other 4 cell lines, in which a strong expression of MP1-MMP was observed, showed a high tendency of invasion (Fig. 4). These invasive cells spread by extending their podocyte into the outer layer (time lapse).

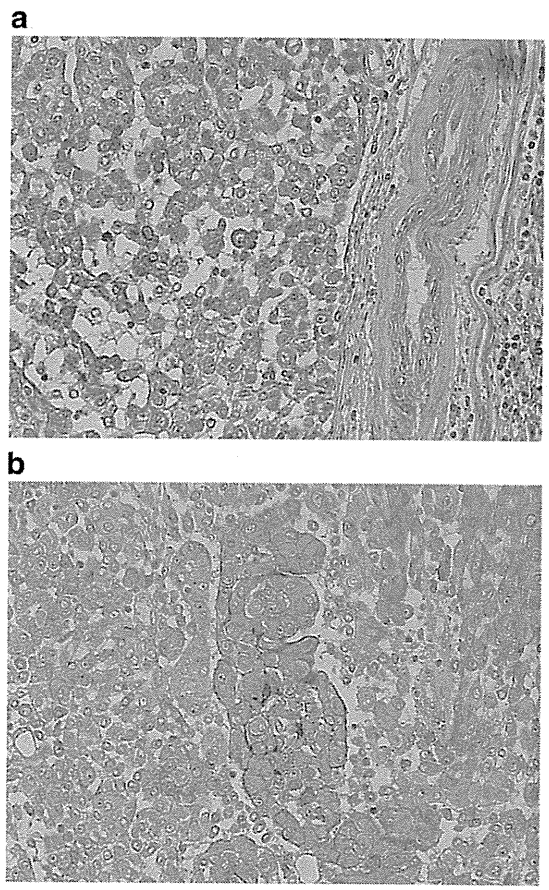

Fig. 2. Result of immunohistochemistry for MT1-MMP using surgical specimens of malignant pleural mesothelioma. Tumor cells expressed MT1-MMP strongly, but the normal vascular endothelial cells did not. (b) Especially, MT1-MMP was more expressed at the edge of the tumor cells than the inner area.

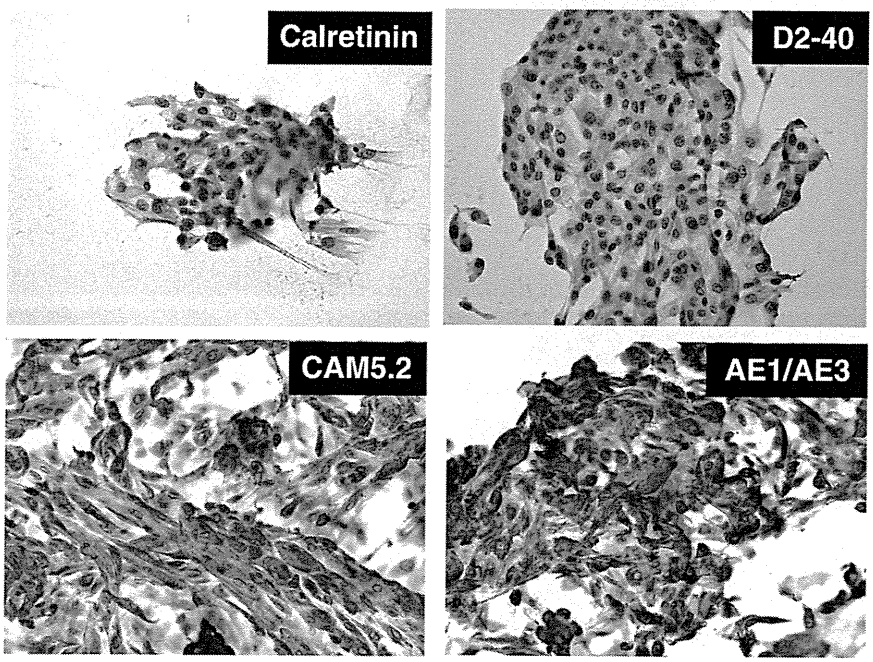

Fig. 1. Cell line established from a sample of malignant pleural mesothelioma. Calretinin, D2-40, CAM5.2, and AE1/AE3 were examined as useful markers of MPM. While D2-40 was not stained, calretinin, AE1/AE3 and CAM5.2 were stained.

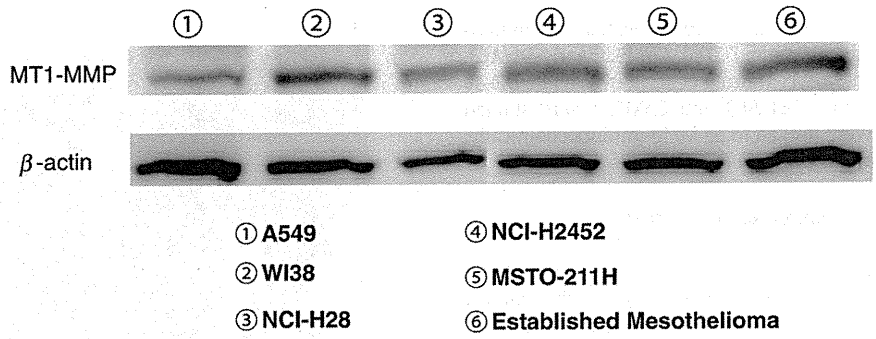

Fig. 3. Western blotting for MT1-MMP and β-actin. We detected a strong expression of MT1-MMP in WI38 and the established MPM cell line. The expression of MT1-MMP was very weak in A549, the cell line of lung adenocarcinoma, and NCI-H28, one of the acquired MPM cell lines. In the other MPM cell lines (NCI-H2452 and MSTO-211H), the expression of MT1-MMP was moderate.

Inhibition of MT1-MMP in the MPM cells and fibroblasts

We performed Western blotting to check if we could inhibit MT1-MMP in WI38 and the established MPM cell line, both of which showed wide spreading in the DL-CGH. The blotting showed about a 50% reduction in the expression of MT1-MMP protein relative to cells transfected with control siRNAs (Fig. 5).

In order to determine their invasive potential cells, transfected with inhibitory RNAs were embedded within the inner layer of DL-CGH and incubated for several days, after which we observed how the cells stained with neutral red. Cells of the established MPM cell line transfected with MT1-MMP RNAi showed only a slight invasion into the outer layer relative to the normal or control RNAi-transfected cells (Fig. 6). We also obtained similar results using WI38 cells (data not shown).

Discussion

In cell culture to establish a primary culture from a clinical specimen is one of the most difficult techniques, so many attempts result in failure. In this study, we succeeded in establishing the MPM cell line with the technique described in Materials and methods.

This is the first study to analyze the invasive activity of cell lines established from clinically resected specimens, with the aim of eventual clinical application. DL-CGH made it possible to visualize the invasive activity of the cells precisely, and the procedure would be useful for deciding a therapeutic strategy and predicting the clinical outcome. Also, the combination of DL-CGH and RNAi treatment of MT1-MMP revealed that the protein was a good candidate for a molecular target that would control the invasive activity of the cancer cells.

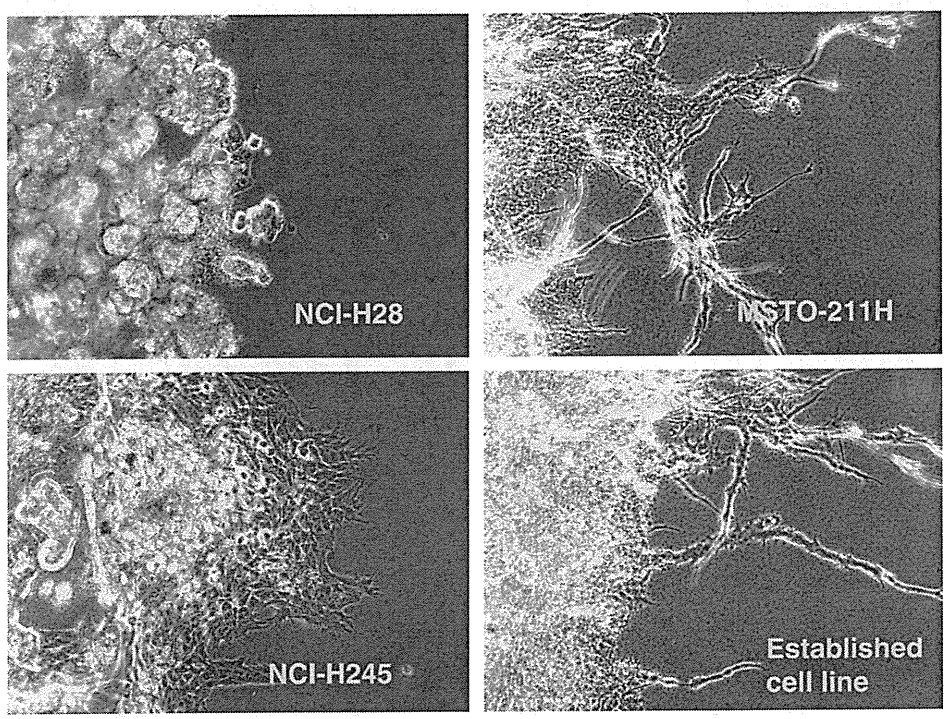

Fig. 4. Invasive activity of malignant mesothelioma cell lines assessed by DL-CGH. NCI-H28, which showed a weak expression of MT1-MMP, showed no tendency to invade the outer layer of collagen gel, whereas the other 3 cell lines showed a high tendency to invade the outer layer.

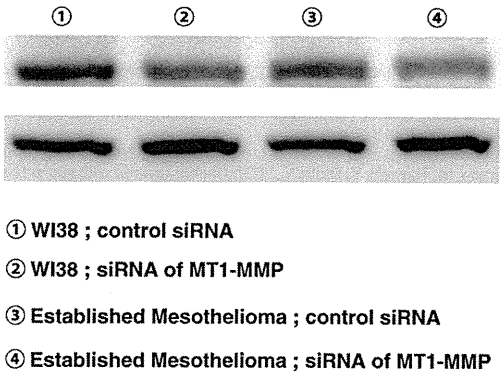

Fig. 5. Western blotting after transfection with siRNA for MT1-MMP. The blotting showed about a 50% reduction in the expression of the MT1-MMP protein relative to cells transfected with control siRNAs.

Invasion occurs within a tumor-host microenvironment, where stroma and tumor cells exchange enzymes and cytokines that modify the local extracellular matrix, stimulate migration, and promote proliferation and survival (Liotta and Kohn, 2001). It has been reported that the presence of fibroblasts is essential in cancer invasion (Olumi et al., 1999; Che et al., 2006; Gaggioli et al., 2007). The fibroblast itself is a benign mesenchymal cell that has no malignancy. Nevertheless, if fibroblasts interact with cancer cells, they play an important role in the tumor cell malignancy. In lung cancer, patients with small-sized bronchiolo-alveolar carcinoma (BAC) of the lung, in which cancer cells spread on the internal surface of alveoli but do not infiltrate interstitially, have a better prognosis than patients with BAC containing actively proliferating fibroblasts; in the latter case, cancer cells invade frequently into micro-vessels (Noguchi et al., 1995). In our study, WI38 cells (a fibroblast cell line) showed the overexpression of MT1-MMP, which indicates that fibroblasts are essential for degenerating the ECM and making tracks and scaffolding for the cancer cells. Not only fibroblasts but also some mesenchymal cells show the overexpression of MT1-MMP. Previous reports have stated that malignant mesothelioma cells produced a broad spectrum of MMPs, which might play an important role in cell invasion (Liu et al., 2001), and that the overexpression of MT1-MMP was observed in malignant mesothelioma (Sivertsen et al., 2006). In the *in vitro* experiments in this study, we observed that the level of MT1-MMP expression in established MPM cells was elevated and that these cells showed active invasion in the assay with DL-CGH.

Cancer-cell migration is typically regulated by integrins, matrix-degrading enzymes, cell–cell adhesion molecules and cell–cell communication (Friedl and Wolf, 2003). Although some tumor cells show sustained protease-independent migration resulting from a flexible amoeba-like shape change (Wolf et al., 2003), it is said that MT1-MMP is the key enzyme in the proteolytic macropatterning of collagen-rich ECM to generate space for the cell masses (Wolf et al., 2007) and that matrix degradation requires MMPs targeted to invadopodia (Sakurai-Yageta et al., 2008). In this study, we were able to establish that the invasive cells spread into the outer layer of the collagen gel by extending their podocyte (dendritic migration). Wolf et al. reported that HT1080 fibrosarcoma showed a spindle-shaped elongation of the cell body for invasion into 3-D collagen matrices (Wolf et al., 2003). We observed a similar phenomenon using the MPM cells and fibroblast. Thus, it is possible that the dendritic migration of mesenchymal cells (such as MPM) results from the overexpression of MT1-MMP.

In conclusion, the overexpression of MT1-MMP in MPM cells is associated with spreading into the surrounding matrix. Furthermore, MT1-MMP expressed in fibroblasts is involved in making a scaffold for the invasion of malignant tumor cells. Thus, we suggest that the degree of MT1-MMP expression is associated with the capacity for locally aggressive spreading into the pleura and the surrounding tissues and that MT1-MMP will be a molecular target for suppressing the invasion of MPM.

Appendix A. Supplementary data

Supplementary data to this article can be found online at doi:10.1016/j.yexmp.2010.10.008.

References

Albini, A., Iwamoto, Y., Kleinman, H.K., Martin, G.R., Aaronson, S.A., Kozlowski, J.M., McEwan, R.N., 1987. A rapid in vitro assay for quantitating the invasive potential of tumor cells. Cancer Res. 47, 3239–3245.

Atkinson, J.M., Pennington, C.J., Martin, S.W., Anikin, V.A., Mearns, A.J., Loadman, P.M., Edwards, D.R., Gill, J.H., 2007. Membrane type matrix metalloproteinases (MMPs) show differential expression in non-small cell lung cancer (NSCLC) compared to normal lung: Correlation of MMP-14 mRNA expression and proteolytic activity. Eur. J. Cancer 43, 1764–1771.

Che, Z.M., Jung, T.H., Choi, J.H., Yoon, D.J., Jeong, H.J., Lee, E.J., Kim, J., 2006. Collagen-based co-culture for invasive study on cancer cells-fibroblasts interaction. Biochem. Biophys. Res. Commun. 346, 268–275.

Curran, S., Murray, G.I., 2000. Matrix metalloproteinases: Molecular aspects of their roles in tumour invasion and metastasis. Eur. J. Cancer 36, 1621–1630.

Duong, H.S., Le, A.D., Zhang, Q., Messadi, D.V., 2005. A novel 3-dimensional culture system as an in vitro model for studying oral cancer cell invasion. Int. J. Exp. Pathol. 86, 365–374.

Edwards, J.G., McLaren, J., Jones, J.L., Waller, D.A., O'Byrne, K.J., 2003. Matrix metalloproteinases 2 and 9 (gelatinases A and B) expression in malignant mesothelioma and benign pleura. Br. J. Cancer 88, 1553–1559.

Friedl, P., Wolf, K., 2003. Tumour-cell invasion and migration: Diversity and escape mechanisms. Nat. Rev. Cancer 3, 362–374.

Gaggioli, C., Hooper, S., Hidalgo-Carcedo, C., Grosse, R., Marshall, J.F., Harrington, K., Sahai, E., 2007. Fibroblast-led collective invasion of carcinoma cells with differing roles for RhoGTPases in leading and following cells. Nat. Cell Biol. 9, 1392–1400.

Konstantinopoulos, P.A., Karamouzis, M.V., Papatsoris, A.G., Papavassiliou, A.G., 2008. Matrix metalloproteinase inhibitors as anticancer agents. Int. J. Biochem. Cell Biol. 40, 1156–1168.

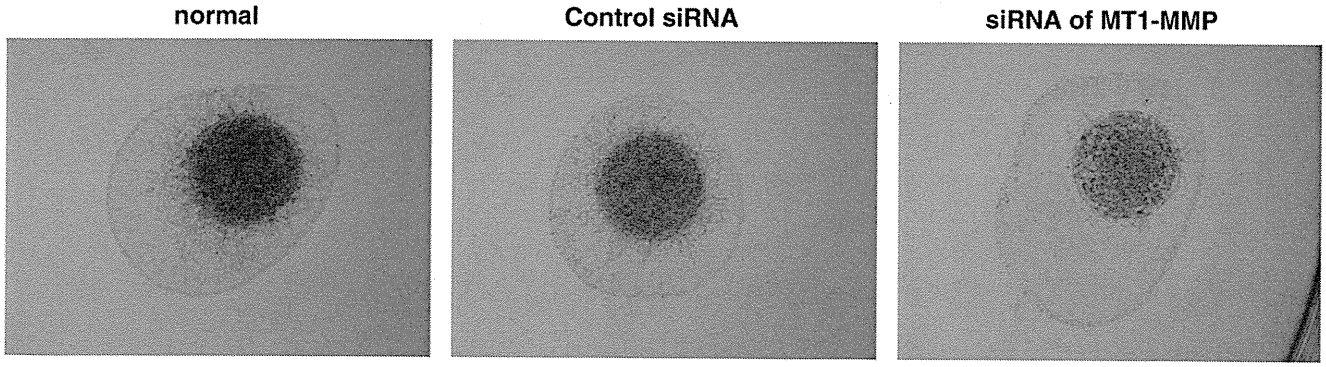

Fig. 6. Result of DL-CGH using MPM cell lines stained with neutral red. In the established MPM cell line, cells transfected with MT1-MMP RNAi showed only a slight invasion into the outer layer relative to that of the normal cells and control-treated cells.

Liotta, L.A., Kohn, E.C., 2001. The microenvironment of the tumour–host interface. Nature 411, 375–379.
Liu, Z., Ivanoff, A., Klominek, J., 2001. Expression and activity of matrix metalloproteases in human malignant mesothelioma cell lines. Int. J. Cancer 91, 638–643.
Mimura, T., Ito, A., Sakuma, T., Ohbayashi, C., Yoshimura, M., Tsubota, N., Okita, Y., Okada, M., 2007. Novel marker D2-40, combined with calretinin, CEA, and TTF-1: An optimal set of immunodiagnostic markers for pleural mesothelioma. Cancer 109, 933–938.
Noguchi, M., Morikawa, A., Kawasaki, M., Matsuno, Y., Yamada, T., Hirohashi, S., Kondo, H., Shimosato, Y., 1995. Small adenocarcinoma of the lung. Histologic characteristics and prognosis. Cancer 75, 2844–2852.
Nyström, M.L., Thomas, G.J., Stone, M., Mackenzie, I.C., Hart, I.R., Marshall, J.F., 2005. Development of a quantitative method to analyse tumour cell invasion in organotypic culture. J. Pathol. 205, 468–475.
Olumi, A.F., Grossfeld, G.D., Hayward, S.W., Carroll, P.R., Tlsty, T.D., Cunha, G.R., 1999. Carcinoma-associated fibroblasts direct tumor progression of initiated human prostatic epithelium. Cancer Res. 59, 5002–5011.
Pistolesi, M., Rusthoven, J., 2004. Malignant pleural mesothelioma: Update, current management, and newer therapeutic strategies. Chest 126, 1318–1329.
Robinson, B.W., Musk, A.W., Lake, R.A., 2005. Malignant mesothelioma. Lancet 366, 397–408.
Sakurai-Yageta, M., Recchi, C., Le Dez, G., Sibarita, J.B., Daviet, L., Camonis, J., D'Souza-Schorey, C., Chavrier, P., 2008. The interaction of IQGAP1 with the exocyst complex is required for tumor cell invasion downstream of Cdc42 and RhoA. J. Cell Biol. 181, 985–998.
Sato, H., Takino, T., Okada, Y., Cao, J., Shinagawa, A., Yamamoto, E., Seiki, M., 1994. A matrix metalloproteinase expressed on the surface of invasive tumour cells. Nature 370, 61–65.
Sivertsen, S., Hadar, R., Elloul, S., Vintman, L., Bedrossian, C., Reich, R., Davidson, B., 2006. Expression of snail, slug and Sip1 in malignant mesothelioma effusions is associated with matrix metalloproteinase, but not with cadherin expression. Lung Cancer 54, 309–317.
Takata, M., Maniwa, Y., Doi, T., Tanaka, Y., Okada, K., Nishio, W., Ohbayashi, C., Yoshimura, M., Hayashi, Y., Okita, Y., 2007. Double-layered collagen gel hemisphere for cell invasion assay: successful visualization and quantification of cell invasion activity. Cell Commun. Adhes. 14, 157–167.
Takino, T., Saeki, H., Miyamori, H., Kudo, T., Sato, H., 2007. Inhibition of membrane-type 1 matrix metalloproteinase at cell-matrix adhesions. Cancer Res. 67, 11621–11629.
Wolf, K., Mazo, I., Leung, H., Engelke, K., von Andrian, U.H., Deryugina, E.I., Strongin, A.Y., Bröcker, E.B., Friedl, P., 2003. Compensation mechanism in tumor cell migration: Mesenchymal-amoeboid transition after blocking of pericellular proteolysis. J. Cell Biol. 160, 267–277.
Wolf, K., Wu, Y.I., Liu, Y., Geiger, J., Tam, E., Overall, C., Stack, M.S., Friedl, P., 2007. Multi-step pericellular proteolysis controls the transition from individual to collective cancer cell invasion. Nat. Cell Biol. 9, 893–904.
Zhong, J., Gencay, M.M., Bubendorf, L., Burgess, J.K., Parson, H., Robinson, B.W., Tamm, M., Black, J.L., Roth, M., 2006. ERK1/2 and p38 MAP kinase control MMP-2, MT1-MMP, and TIMP action and affect cell migration: A comparison between mesothelioma and mesothelial cells. J. Cell Physiol. 207, 540–552.

Cancer Science
The official journal of the Japanese Cancer Association

Oncogenic phosphatase Wip1 is a novel prognostic marker for lung adenocarcinoma patient survival

Naoyuki Satoh,[1] Yoshimasa Maniwa,[2,7] Vladimir P. Bermudez,[3] Kunihiro Nishimura,[4] Wataru Nishio,[2] Masahiro Yoshimura,[2] Yutaka Okita,[5] Chiho Ohbayashi,[6] Jerard Hurwitz[3] and Yoshitake Hayashi[1]

[1]Division of Molecular Medicine and Medical Genetics, Department of Pathology, Divisions of [2]Thoracic Surgery, [3]Evidence-Based Laboratory Medicine, [4]Cardiovascular Surgery, [5]Cancer Pathology, Department of Pathology, Kobe University Graduate School of Medicine, Kobe, Japan; [6]Program in Molecular Biology, Sloan-Kettering Institute, Memorial Sloan-Kettering Cancer Center, New York, New York, USA

(Received September 22, 2010/Revised January 20, 2011/Accepted January 21, 2011/Accepted manuscript online February 1, 2011/Article first published online March 4, 2011)

DNA damage response pathways are important for maintaining genomic stability. The oncogenic phosphatase Wip1 plays a crucial role in DNA damage response by inhibiting several cell cycle proteins, including p53. Although *Wip1* gene amplification has been reported in various primary tumors, including lung cancer, its biological significance for survival of primary lung tumor patients remains unclear. We investigated the expression of Wip1 in cancer epithelial cells immunohistochemically in 84 consecutive resected cases of lung adenocarcinoma. Increased Wip1 expression was observed in 54 (64.3%) of the 84 cases. Wip1 expression was found to be correlated significantly with two clinicopathological factors: γ-H2AX expression, and invasion to the pulmonary vein. A univariate analysis and log–rank test indicated a significant association between Wip1 expression and lower overall survival rate ($P = 0.019$ and $P = 0.0099$, respectively). A multivariate analysis also indicated a statistically significant association between increased Wip1 expression and lower overall survival rate (hazard ratio, 4.3; $P = 0.026$). The Ki67 index level was higher in the Wip1-positive group than in the negative group ($P < 0.04$, Mann–Whitney *U*-test). Moreover, in a subgroup analysis of only stage I patients, increased Wip1 expression was also significantly associated with a lower overall survival rate ($P = 0.023$, log–rank test). These results indicate that the increased expression of Wip1 in cancer epithelial cells has significant value for tumor progression and the clinical prognosis of patients with primary lung adenocarcinoma. (*Cancer Sci* 2011; 102: 1101–1106)

Cellular DNA is constantly exposed to various environmental and endogenous mutagenic insults. To maintain genomic integrity and prevent cancers caused by these potentially mutagenic events, a sophisticated array of damage sensors, signaling molecules, and repair functions have evolved. Among the key sensors of DNA damage are the phosphoinositide-3-kinase-related kinase family, which includes ATM (ataxia-telangiectasia mutated), ATR (ataxia-telangiectasia and Rad3-related), and DNA-PK_{cs} (DNA-dependent protein kinase catalytic subunit).[1,2] A direct role for the ATM/ATR-initiated damage response pathways in cancer prevention has been recently determined.[3,4] Human pre-neoplastic lesions from a variety of different human cancers were shown to express various markers reflecting responses to DNA damage response, including activated and phosphorylated ATM, Chk2, p53, and H2AX.[3,4] In particular, phosphorylated H2AX (called γ-H2AX) plays a crucial role in recruiting DNA damage response factors to damage sites for accurate DNA repair and is considered a specific and sensitive molecular marker of DNA damage and repair.[5–7] Interestingly, late-stage tumors often show loss of these DNA damage response markers, suggesting that a decrease in the activity of DNA damage response pathways may contribute to cancer progression.[3,4]

Wild-type p53-induced phosphatase 1 (Wip1), also called PPM1D, is a member of the magnesium-dependent serine/threonine protein phosphatase (PPM) family.[8] These proteins, whose defining member is PP2Cα, are present in both prokaryotes and eukaryotes.[9] The human *Wip1* gene was first identified as a transcript induced by ultraviolet and ionizing radiation in a p53-dependent manner.[10] To date, Wip1 has been shown to dephosphorylate at least six proteins, ATM, Chk1, Chk2, p53, p38, and Mdm2.[11] A number of studies have shown that the Wip1 phosphatase is a key integrator of a response that attenuates signaling through the ATM and ATR pathways and negatively regulates the stress-responsive p38 MAPK pathway.[11] Furthermore, several reports recently showed that Wip1 directly dephosphorylated γ-H2AX, which might result in attenuating the DNA damage response.[12,13] Thus, Wip1 is considered to be an inhibitor or homeostatic regulator of the DNA damage response that facilitates the return of cells to a normal pre-stress state following DNA damage repair.

In addition, Wip1 is regarded as an oncogenic phosphatase because of the above noted functions. Indeed, amplified levels of *Wip1* have been found in cancer cell lines of the lung, breast, pancreas, bladder, liver, and meninges, and neuroblastomas.[14,15] Moreover, a number of human primary tumors (e.g., breast adenocarcinoma, ovarian clear cell adenocarcinoma, neuroblastoma, and pancreatic adenocarcinoma) contain amplified *Wip1* gene and high levels of Wip1 protein, which appear to correlate with poor prognosis for cancer patients.[16–19] However, it is still unknown whether Wip1 overexpression affects the survival of primary lung carcinoma patients. In this study, we analyzed the expression of Wip1 by immunohistochemistry in surgically resected human primary pulmonary adenocarcinoma tissue from 84 patients. We also investigated whether Wip1 expression in tumor tissues influenced the outcome of these patients.

Materials and Methods

Collection of samples and patient data. Eighty-four patients (46 males, 38 females) examined and treated at Kobe University Hospital (Kobe City, Japan) between 2001 and 2003 for lung adenocarcinoma were evaluated for this study. The study was approved by the Regional Ethics Committee for Clinical Research of Kobe University and conducted according to the principles in the Declaration of Helsinki. All patients gave dated and written informed consent. Primary tumors and adjacent non-neoplastic lung tissue were obtained at the time of surgery. Peripheral portions of resected lung carcinomas were sectioned, evaluated by a pathologist, and used for immunohistochemistry (IHC).

[7]To whom correspondence should be addressed.
E-mail: maniwa@med.kobe-u.ac.jp

doi: 10.1111/j.1349-7006.2011.01898.x

All patients were consecutively enrolled in this study. Detailed clinical and demographic information, prognostic factors, and disease progression were collected retrospectively.

Immunohistochemistry. Formalin-fixed paraffin-embedded specimens were sectioned in 5 μm-thick slices and sections were deparaffinized with xylene and rehydrated with ethanol. Antigen retrieval was carried out by placing specimens in Dako REAL Target Retrieval Solution (Dako, Glostrup, Denmark) at 98°C for 20 min. Rabbit anti-human Wip1 polyclonal antibodies (1:100; Santa Cruz Biotechnology, Santa Cruz, CA, USA) and rabbit anti-human phospho-histone H2AX (S139) polyclonal antibodies (5 μg/mL; R&D Systems, Minneapolis, MN, USA) were used as the primary antibodies for detection of Wip1 and γ-H2AX, respectively. The Dako EnVision/HRP Universal (DAB) kit (Dako) was used for endogenous peroxidase blocking, treatment with a secondary antibody against anti-rabbit and anti-mouse immunoglobulin antibody, and the visualization of HRP. Hematoxylin staining was used as the counterstain. Photographs of immunohistochemical stained sections were taken by a camera mounted on a Keyence BZ-8000 digital microscope (Keyence, Osaka, Japan).

Detection of *EGFR* gene mutation. Genomic DNA of tumor cells was successfully extracted from 19 paraffin-embedded tissue specimens.[20] *EGFR* gene (exons 18–21) of the DNA samples was investigated by the peptide nucleic acid-locked nucleic acid PCR clamp method.[21]

Classification of immunohistochemically stained patterns. Immunochemically stained sections were classified by light microscopy. For the assessment of the protein expression of Wip1, samples were classified as Wip1-positive if the ratio of stained cells in total epithelial cancer cells of a tumor tissue was more than 10%; if samples contained <10% stained cells, they were classified as Wip1-negative. Ten percent was used as the cut-off value because of the statistical advantage in this study. For evaluation of γ-H2AX expression, the cut-off value (the ratio of stained cells in total epithelial cancer cells) was set at 3% to obtain high sensitivity for detecting DNA damage. Sample classification was done independently by two pathologists (C.O. and Y.H.) in a blind manner. Ki67 (MIB-1) index (Ki67 expression ratio) and tumor protein p53 (TP53) expression were determined by the Division of Diagnostic Pathology, Kobe University.

Statistical analysis. All statistical analyses were carried out using Stata software version 10.1 (Stata, College Station, TX, USA). Baseline characteristics were reported as percentages for categorical variables and means for ±SD for continuous variables. Fisher's exact or Student's *t*-test were used to examine the association between Wip1 expression and various clinicopathological parameters. For survival analyses, we used the Kaplan–Meier method, and statistical significance between survival curves was assessed by the log–rank test. Overall survival (OS) and relapse-free interval (RFI) were determined from the date of surgery to the time of death or relapse, respectively. The Cox proportional hazards model was used to examine the association between the OS and the RFI and potential prognostic factors. Data were censored at the time of last visit. Significant variables from the univariate analysis were entered into the Cox hazard model analysis. Probability values <0.05 were considered statistically significant in all analyses.

Results

Wip1 expression in epithelial cancer cells of human lung adenocarcinoma. The expression of Wip1 was examined in 84 lung adenocarcinomas and the adjacent normal lung tissues by IHC using anti-human Wip1 polyclonal antibodies. In normal lung tissues, the expression of Wip1 was not detected (Fig. 1A). In some tumor tissues, Wip1 expression was observed in cancer cells (Fig. 1B–D). The frequency of Wip1-stained samples was 64.3% of all samples examined (54/84).

Relationship between Wip1 expression and clinicopathological characteristics of patients. For assessment purposes, we regarded specimens as Wip1 positive if 10% or more cancer cells within a tumor were strongly stained; all other specimens were regarded as negative. Based on this, 54 specimens were classified as Wip1 positive (64.3%) and 30 specimens as Wip1 negative (35.7%).

The relationships between Wip1-positive cases and various clinicopathological characteristics at the time of surgery are shown in Table 1. Expression of γ-H2AX was observed in 38 of 84 specimens (45.2%). Increased expression of Wip1 was significantly associated with γ-H2AX expression ($P < 0.001$) and cancer invasion to the pulmonary vein ($P = 0.019$). Wip1 expression was not significantly related to age ($P = 0.59$),

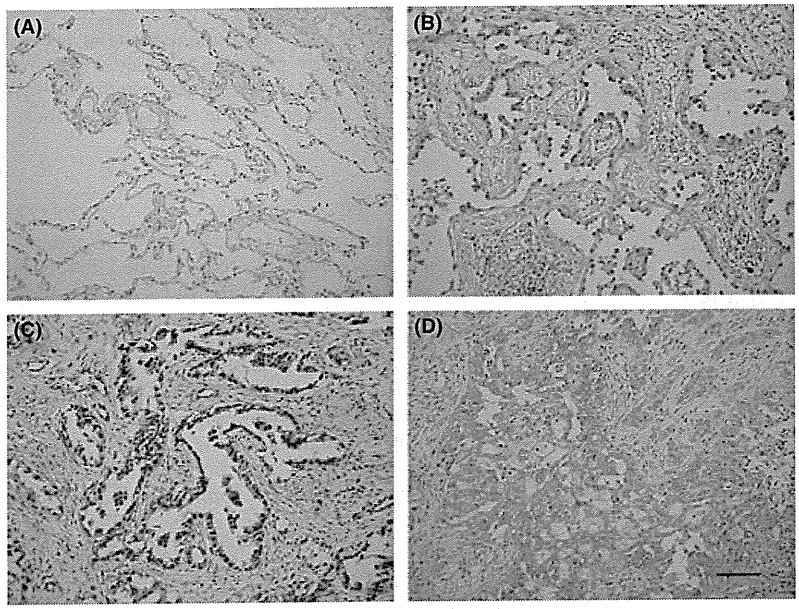

Fig. 1. Immunohistochemical analysis of expression of oncogenic phosphatase Wip1 in epithelial cancer cells of human primary lung adenocarcinoma. (A) Wip1-negative normal lung tissue. (B) Wip1-negative tumor tissue. Cancer cells were not stained. (C,D) Wip1-positive tumor tissues. Cancer cells were diffusely stained. Scale line = 100 μm (magnification, ×200).

doi: 10.1111/j.1349-7006.2011.01898.x

Table 1. Association between increased expression of oncogenic phosphatase Wip1 and clinicopathologic characteristics in 84 patients with lung adenocarcinoma

Variable	Total	Wip1		*P*-value
		Negative	Positive	
No. patients (%)	84	30 (35.7)	54 (64.3)	NA
Age in years, mean ± SD (range)	67.3 ± 9.1 (42–81)	68.0 ± 8.5 (49–80)	66.9 ± 9.5 (42–81)	0.59*
Gender				
Male/female	46/38	19/11	27/27	0.26
T factor				
T1/T2/T3/T4	45/31/3/4†	20/10/0/0	25/21/3/4	0.17
N factor				
N0/N1/N2/N3	59/8/15/1†	24/3/3/0	35/5/12/1	0.49
M factor				
M0/M1	82/1†	30/0	52/1	1.0
Stage				
I/II/III, IV	56/10/17†	24/3/3	32/7/14	0.14
P factor				
0/1/2/3	56/14/10/4	23/4/3/0	33/10/7/4	0.43
PA invasion				
Negative/positive	67/15‡	26/3	41/12	0.24
PV invasion				
Negative/positive	47/35‡	22/7	25/28	0.019
LY invasion				
Negative/positive	50/32‡	22/7	28/25	0.058
TP53 expression				
Negative/positive	45/39	16/14	29/25	1.0
γ-H2AX expression				
Negative/positive	46/38	25/5	21/33	<0.001

*P-value by Student's *t*-test. Fisher's exact test was used for statistical analysis. †One sample missing. ‡Two samples missing. LY, lymphatic duct; NA, not applicable; PA, pulmonary artery; PV, pulmonary vein.

gender ($P = 0.26$), TNM stage ($P = 0.14$), T factor ($P = 0.17$), P factor ($P = 0.43$) according to the criteria of the International Staging System for Lung Cancer, lymph node metastasis (0.49), distant metastasis ($P = 1.0$), cancer invasion to the pulmonary artery ($P = 0.24$) or the lymphatic ducts ($P = 0.058$), or TP53 expression ($P = 1.0$). *EGFR* mutation was detected in 6 of 19 samples (31.6%). Wip1 expression was not significantly related to *EGFR* mutation (three samples with *EGFR* mutation in nine Wip1-negative samples and 3 in 10 Wip1-positive samples; 33.3% and 30.0%, respectively; $P = 1.0$).

Increased expression of Wip1 related to poor patient prognosis and proliferation of cancer cells. Using the data collected from 84 study patients, we evaluated their prognosis and its relationship to the expression of Wip1. We examined the OS of Wip1-negative and Wip1-positive groups and found a statistically significant difference between the two groups using the log–rank test ($P = 0.0099$). As shown, survival of Wip1-negative patients was greater than that observed for Wip1-positive patients (Fig. 2). Moreover, using the Mann–Whitney *U*-test, the Ki67 index level was higher in the Wip1-positive group than in the negative group (Fig. 3). The median Ki67 index was 6% and 10% in Wip1-negative and Wip1-positive tumors, respectively. A univariate analysis indicated that among clinicopathological factors, tumor classification, lymph node metastasis, and increased Wip1 expression correlated with outcome (Table 2). Further assessment using the Cox multivariate analysis indicated that gender (male), lymph node metastasis, and increased Wip1 expression were statistically significant predictors for OS (Table 2).

We also analyzed the RFI rate for increased Wip1 expression. In our study, the RFI rate in patients positive for increased Wip1 expression was notably lower than that in the negative group ($P = 0.013$, log–rank test; data not shown). Univariate analysis of RFI also indicated that increased Wip1 expression correlated with outcome ($P = 0.018$, hazard ratio; 2.9, 95% CI; 1.2–7.2).

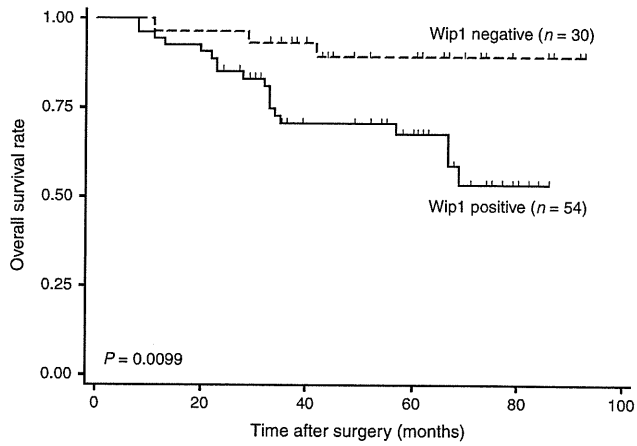

Fig. 2. Kaplan–Meier plot of the overall survival rate in 84 patients with lung adenocarcinoma, and its relationship to expression of oncogenic phosphatase Wip1. *P*-value determined using the log–rank test.

Increased expression of Wip1 also related to poor patient prognosis in stage I lung adenocarcinoma. In the stage I cases, 32 (57.1%) and 24 (42.9%) patients were classified as Wip1 positive and Wip1 negative, respectively (Table 1). A survival analysis that included only stage I patients revealed that the overall survival curve for the Wip1-positive group was lower than the Wip1-negative group. The log–rank test showed that the difference was statistically significant ($P = 0.023$) (Fig. 4).

Discussion

In the present study, we carried out IHC staining of human primary adenocarcinoma tissue specimens to detect the protein

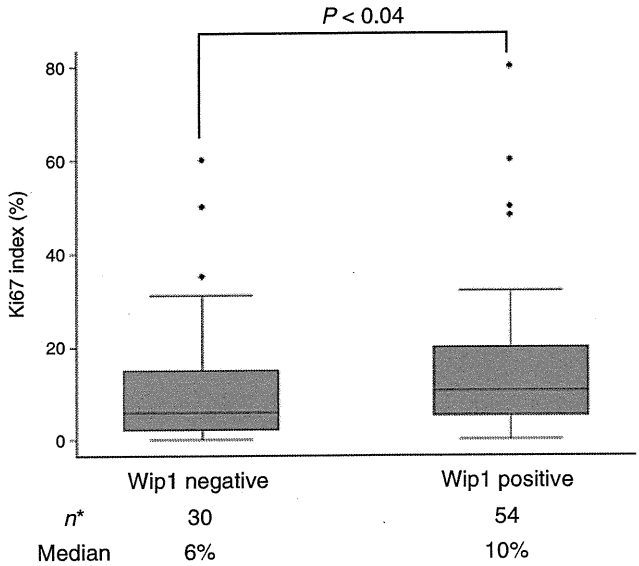

Fig. 3. Ki67 index (%) in lung adenocarcinoma samples and its relationship to the expression of oncogenic phosphatase Wip1. *P*-value determined using the Mann–Whitney *U*-test. **n*, number of lung tumors.

Table 2. Univariate and multivariate analysis of the association between the overall survival of 84 patients with lung adenocarcinoma and prognostic factors, by Cox proportional hazard models

Variable	Hazard ratio	95% Confidence interval	*P*-value
Univariate			
Age	1.0	1.3–14.6	0.93
Gender (male *versus* female)	0.51	0.21–1.3	0.14
T factor (T1<)	2.9	1.2–7.1	0.021
LN (negative *versus* positive)	3.8	1.6–8.9	0.002
PV invasion (negative *versus* positive)	2.2	0.92–5.1	0.077
Wip1 (negative *versus* positive)	4.3	1.3–14.6	0.019
Multivariate			
Age	1.0	0.97–1.1	0.42
Gender (male *versus* female)	0.31	0.11–0.84	0.031
T factor (T1<)	2.2	0.81–5.9	0.12
LN (negative *versus* positive)	3.4	1.3–9.2	0.015
PV (negative *versus* positive)	0.63	0.21–1.9	0.42
Wip1 (negative *versus* positive)	4.3	1.2–15.6	0.026

LN, lymph node metastasis; PV, invasion to pulmonary vein.

expression of oncogenic phosphatase Wip1 and observed the increased expression of Wip1 in tumor tissues, but not in normal lung tissues. The increased Wip1 expression was associated significantly with lower overall survival rate of lung adenocarcinoma patients. To our knowledge, this is the first study to detect protein expression of Wip1 in lung adenocarcinoma and to report that Wip1 expression might be a useful prognostic marker for lung adenocarcinoma patient survival.

Using IHC staining, increased Wip1 protein expression was observed in 64.3% (54/84) of lung adenocarcinoma specimens but was not detected in adjacent non-neoplastic lung tissues (Fig. 1). In order to define the effects of increased Wip1 expression on the prognosis of patients with lung cancer, a prognostic analysis was carried out on follow-up data. The results of the

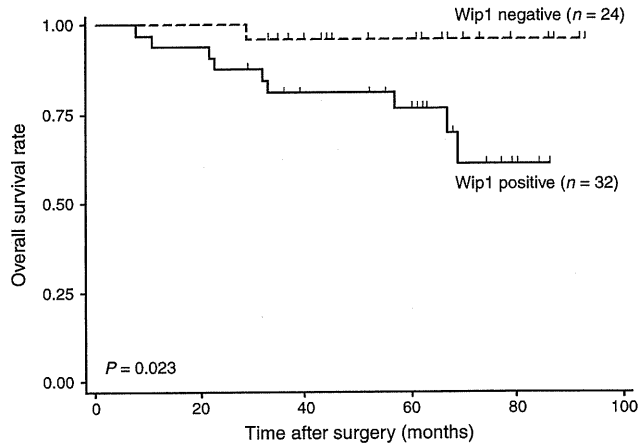

Fig. 4. Kaplan–Meier plot of the overall survival rate in 84 patients with lung adenocarcinoma and its relationship to expression of oncogenic phosphatase Wip1 in stage I patients. *P*-value determined using the log–rank test.

survival analysis showed that the OS rate in patients positive for increased Wip1 expression was notably lower than that of the Wip1-negative group (Fig. 2). These findings indicate that increased Wip1 expression negatively affects the clinical course and that increased Wip1 expression is correlated with malignant behavior of tumors. Our Cox multivariate analysis indicated that increased Wip1 expression, gender (male), and lymph node metastasis were significant prognostic predictors. It has been reported that once lung adenocarcinoma was resected completely, women survived longer than male patients.[22] Furthermore, a prognostic analysis that included only stage I cases revealed that the OS rate of the Wip1-positive group was significantly lower than that of the Wip1-negative group. These findings suggest that increased Wip1 expression may be used as a reference index for molecular staging of patients with a high risk of death who are likely to benefit from intensive adjuvant therapy.

A number of recent reports indicate that Wip1 overexpression in mouse embryonic fibloblasts and transgenic mice promotes cell transformation and accelerated cancer progression.[14,23,24] Furthermore, *Wip1*-disrupted mice are resistant to mammary cancer, and even when tumors form in such mice, their tumor cells have a lower proliferation potential.[15] It has been suggested that the effects of Wip1 overexpression might be due to its dephosphorylation of p38, p53, and regulators of p53 (ATM, Chk1, Chk2).[11] Although the direct downstream effector of Wip1 leading to tumor progression is still unclear, we consider it more likely that increased Wip1 expression contributes to cell proliferation. For this reason, we examined the relationship between increased Wip1 expression and cell proliferation. As an indicator of cell proliferation, we used the Ki67 (MIB-1) expression index (determined by pathologists in the Division of Diagnostic Pathology, Kobe University). Using the Mann–Whitney *U*-test, the Ki67 index level was higher in the Wip1-positive group than in the negative group (Fig. 3). Moreover, the size of tumors (mm^3) was slightly greater in the Wip1-positive group than in the negative group ($P = 0.062$, Mann–Whitney *U*-test, median; 12.0 *vs* 8.4 mm^3, data not shown). In the stage I patients, the Ki67 index levels tended to be higher in the Wip1-positive group than in the negative group ($P = 0.084$, Mann–Whitney *U*-test, data not shown). In our study, increased expression of Wip1 was significantly associated with cancer invasion to the pulmonary vein ($P = 0.019$) and tended to be related to cancer invasion to the pulmonary lymphatic vessel ($P = 0.058$; Table 2). These

doi: 10.1111/j.1349-7006.2011.01898.x

results suggest that increased Wip1 expression may enhance cancer cell proliferation and tumor progression, resulted in cancer invasion to the tumor vessels.

Multiple studies showed that continuous formation of DNA double-strand breaks might contribute to increased genomic instability, leading to tumorigenesis, because of breach of a barrier (such as DNA damage response including *p53* activation).[3,4,25,26] In this study, IHC staining of γ-H2AX protein was carried out to detect presence of DNA damage in the tumor tissues and γ-H2AX expression was observed in 38 of 84 samples (45.2%; Table 1). Interestingly, our result showed that increased expression of Wip1 was significantly associated with γ-H2AX expression ($P < 0.001$). In the presence of DNA damage (indicated by γ-H2AX expression), Wip1 expression might be activated in the process of DNA damage response.[11] It is still unknown whether increased Wip1 expression results from genomic instability or not, and further studies will be required to substantiate these notions.

Alterations of the p53 tumor suppressor gene are the most common genetic changes found in human malignancies, including lung cancer.[27] Although a number of clinical prognostic studies of p53 mutations in lung cancer have been reported, using either IHC or molecular analysis, their effects on survival are unclear. Most studies suggest that the prognosis of patients with mutations in p53 are poorer than those devoid of such alterations,[28] however, others have reported an opposite relationship.[29,30] In our study, overexpression of mutated p53 was observed in 39 of 84 (46.4%) lung adenocarcinoma specimens (Table 1). However, the presence of mutated p53 did not significantly affect the overall survival rate ($P = 0.85$, data not shown). It was previously reported that only one of eight primary breast tumors with elevated levels of Wip1 showed p53 mutations and that Wip1 overexpression correlated with a poor prognosis despite the absence of p53 mutations in the same tumor.[14] In our studies (using IHC staining) we did not observe any association between increased Wip1 expression and p53 mutations in lung adenocarcinoma (Table 1). Recently, it has been reported that activating mutations of *EGFR* are present in a subset of pulmonary adenocarcinomas and also prognostic for survival benefit.[31,32] In this study, *EGFR* mutation was detected in 6 of 19 lung adenocarcinomas (31.6%) and increased Wip1 expression was not significantly related to *EGFR* mutation (three samples with *EGFR* mutation of nine Wip1-negative samples and 3 of 10 Wip1-positive samples; 33.3% and 30.0%, respectively; $P = 1.0$). These results suggest that Wip1 expression itself was not directly related to development of EGFR mutation.

It has been recently reported that p38α MAPK is essential for both proliferation and differentiation of lung stem and progenitor cells, and that the downregulation of p38α might result in human lung tumorigenesis.[33] According to these results, p38 MAPK that is dephosphorylated by Wip1 can negatively regulate the action of EGFR in the proliferation and self-renewal of lung stem and progenitor cells. Interestingly, p38 protein expression was approximately three times lower in human lung tumor samples than that found in normal lung tissues. Thus, p38 dephosphorylation, resulting in upregulation of EGFR, might explain why Wip1 enhances the progression and malignancy of lung adenocarcinoma. Although the downstream factor(s) in the Wip1 pathway that can explain the relationship between increased Wip1 expression and poor prognosis of lung adenocarcinoma patients is presently unknown, dephosphorylation of p38, p53, and γ-H2AX by Wip1 may contribute importantly to tumorigenesis and tumor progression. Thus, Wip1 might be a new lung cancer therapy target.

In conclusion, our results suggest that increased Wip1 expression in cancer cells in primary lung adenocarcinoma plays an important role in the progression of lung adenocarcinoma and acts as a negative factor for the prognosis of patients. These results suggest that increased expression of Wip1 can be used as a reference index of molecular staging to select patients at high risk of death as well as relapsed patients who may benefit from intensive adjuvant therapy.

Disclosure Statement

None of the authors have any interests which may be perceived as posing a conflict or bias.

References

1 Abraham RT. Cell cycle checkpoint signaling through the ATM and ATR kinases. *Genes Dev* 2001; **15**: 2177–96.
2 Shiloh Y. ATM and related protein kinase: safeguarding genome integrity. *Nat Rev Cancer* 2003; **3**: 155–68.
3 Gorgoulis VG, Vassiliou LV, Karakaidos P *et al.* Activation of the DNA damage checkpoint and genomic instability in human precancerous lesions. *Nature* 2005; **434**: 907–13.
4 Bartkova J, Horejsí Z, Koed K *et al.* DNA damage response as a candidate anti-cancer barrier in early human tumorigenesis. *Nature* 2005; **434**: 864–70.
5 Bonner WM, Redon CE, Dickey JS *et al.* γH2AX and cancer. *Nat Rev Cancer* 2008; **8**: 957–67.
6 Mah LJ, El-Osta A, Karagiannis TC. γH2AX: a sensitive molecular marker of DNA damage and repair. *Leukemia* 2010; **24**: 679–86.
7 Yu T, MacPhail SH, Banáth JP *et al.* Endogenous expression of phosphorylated histone H2AX in tumors in relation to DNA double-strand breaks and genomic instability. *DNA Repair (Amst)* 2006; **5**: 935–46.
8 Moorhead GB, Trinkle-Mulcahy L, Ulke-Lemée A. Emerging roles of nuclear protein phosphatases. *Nat Rev Mol Cell Biol* 2007; **8**: 234–44.
9 Jackson MD, Denu JM. Molecular reactions of protein phosphatases – insights from structure and chemistry. *Chem Rev* 2001; **101**: 2313–40.
10 Fiscella M, Zhang H, Fan S *et al.* Wip1, a novel human protein phosphatase that is induced in response to ionizing radiation in a p53-dependent manner. *Proc Natl Acad Sci U S A* 1997; **94**: 6048–53.
11 Lu X, Nguyen TA, Moon SH *et al.* The type 2C phosphatase Wip1: an oncogenic regulator of tumor suppressor and DNA damage response pathways. *Cancer Metastasis Rev* 2008; **27**: 123–35.
12 Cha H, Lowe JM, Li H *et al.* Wip1 directly dephosphorylates γ-H2AX and attenuates the DNA damage response. *Cancer Res* 2010; **70**: 4112–22.
13 Moon SH, Lin L, Zhang X *et al.* Wild-type p53-induced phosphatase 1 dephosphorylates histone variant γ-H2AX and suppresses DNA double strand break repair. *J Biol Chem* 2010; **285**: 12935–47.
14 Bulavin DV, Demidov ON, Saito S *et al.* Amplification of PPM1D in human tumors abrogates p53 tumor-suppressor activity. *Nat Genet* 2002; **31**: 210–5.
15 Bulavin DV, Phillips C, Nannenga B *et al.* Inactivation of the Wip1 phosphatase inhibits mammary tumorigenesis through p38 MAPK-mediated activation of the p16(Ink4a)-p19(Arf) pathway. *Nat Genet* 2004; **36**: 343–50.
16 Rauta J, Alarmo EL, Kauraniemi P *et al.* The serine-threonine protein phosphatase PPM1D is frequently activated through amplification in aggressive primary breast tumours. *Breast Cancer Res Treat* 2006; **95**: 257–63.
17 Hirasawa A, Saito-Ohara F, Inoue J *et al.* Association of 17q21-q24 gain in ovarian clear cell adenocarcinomas with poor prognosis and identification of PPM1D and APPBP2 as likely amplification targets. *Clin Cancer Res* 2003; **9**: 1995–2004.
18 Saito-Ohara F, Imoto I, Inoue J *et al.* PPM1D is a potential target for 17q gain in neuroblastoma. *Cancer Res* 2003; **63**: 1876–83.
19 Loukopoulos P, Shibata T, Katoh H *et al.* Genome-wide array-based comparative genomic hybridization analysis of pancreatic adenocarcinoma: identification of genetic indicators that predict patient outcome. *Cancer Sci* 2007; **98**: 392–400.
20 Coombs NJ, Gough AC, Primrose JN. Optimisation of DNA and RNA extraction from archival formalin-fixed tissue. *Nucleic Acids Res* 1999; **27**: e12.
21 Nagai Y, Miyazawa H, Huqun *et al.* Genetic heterogeneity of the epidermal growth factor receptor in non-small cell lung cancer cell lines revealed by a rapid and sensitive detection system, the peptide nucleic acid-locked nucleic acid PCR clamp. *Cancer Res* 2005; **65**: 7276–82.
22 Minami H, Yoshimura M, Miyamoto Y *et al.* Lung cancer in women: sex-associated differences in survival of patients undergoing resection for lung cancer. *Chest* 2000; **118**: 1603–9.

23 Nannenga B, Lu X, Dumble M *et al.* Augmented cancer resistance and DNA damage response phenotypes in PPM1D null mice. *Mol Carcinog* 2006; **45**: 594–604.
24 Demidov ON, Kek C, Shreeram S *et al.* The role of the MKK6/p38 MAPK pathway in Wip1-dependent regulation of ErbB2-driven mammary gland tumorigenesis. *Oncogene* 2007; **26**: 2502–6.
25 Halazonetis TD, Gorgoulis VG, Bartek J. An oncogene-induced DNA damage model for cancer development. *Science* 2008; **319**: 1352–5.
26 Beckman RA, Loeb LA. Efficiency of carcinogenesis with and without a mutator mutation. *Proc Natl Acad Sci U S A* 2006; **103**: 14140–5.
27 Bennett WP, Hussain SP, Vahakangas KH *et al.* Molecular epidemiology of human cancer risk: gene-environment interactions and p53 mutation spectrum in human lung cancer. *J Pathol* 1999; **187**: 8–18.
28 Campling BG, El-Deiry WS. Clinical implication of p53 mutation in lung cancer. *Mol Biotechnol* 2003; **24**: 141–56.
29 Passlick B, Izbicki JR, Riethmüller G *et al.* p53 in non-small-cell lung cancer. *J Natl Cancer Inst* 1994; **86**: 801–3.
30 Lee JS, Yoon A, Kalapurakal SK *et al.* Expression of p53 oncoprotein in non-small-cell lung cancer: a favorable prognostic factor. *J Clin Oncol* 1995; **13**: 1893–903.
31 Mitsudomi T, Kosaka T, Endoh H *et al.* Mutations of the epidermal growth factor receptor gene predict prolonged survival after gefitinib treatment in patients with non-small-cell lung cancer with postoperative recurrence. *J Clin Oncol* 2005; **23**: 2513–20.
32 Kosaka T, Yatabe Y, Onozato R *et al.* Prognostic implication of EGFR, KRAS, and TP53 gene mutations in a large cohort of Japanese patients with surgically treated lung adenocarcinoma. *J Thorac Oncol* 2009; **4**: 22–9.
33 Ventura JJ, Tenbaum S, Perdiguero E *et al.* p38alpha MAP kinase is essential in lung stem and progenitor cell proliferation and differentiation. *Nat Genet* 2007; **39**: 750–8.

doi: 10.1111/j.1349-7006.2011.01898.x

European Journal of Radiology 77 (2011) 97–104

Contents lists available at ScienceDirect

European Journal of Radiology

journal homepage: www.elsevier.com/locate/ejrad

State-of-the-art radiological techniques improve the assessment of postoperative lung function in patients with non-small cell lung cancer☆

Yoshiharu Ohno[a,*], Hisanobu Koyama[a], Munenobu Nogami[a,b], Daisuke Takenaka[a], Yumiko Onishi[a], Keiko Matsumoto[a], Sumiaki Matsumoto[a], Yoshimasa Maniwa[c], Masahiro Yoshimura[c,d], Yoshihiro Nishimura[e], Kazuro Sugimura[a]

[a] Department of Radiology, Kobe University Graduate School of Medicine, 7-5-2 Kusunoki-cho, Chuo-ku, Kobe, Hyogo 650-0017, Japan
[b] Division of Image-Based Medicine, Institute of Biomedical Research and Innovation, 2-2 Minatojima Minami-machi, Chuo-ku, Kobe, Hyogo, 650-0047, Japan
[c] Division of Cardiovascular, Thoracic and Pediatric Surgery, Kobe University Graduate School of Medicine, 7-5-2 Kusunoki-cho, Chuo-ku, Kobe, Hyogo, 650-0017, Japan
[d] Division of Thoracic Surgery, Hyogo Cancer Center, 13-7 Kitaohji-cho, Akashi, Hyogo, 673-8558, Japan
[e] Division of Respiratory Medicine, Department of Internal Medicine, Kobe University Graduate School of Medicine, 7-5-2 Kusunoki-cho, Chuo-ku, Kobe, Hyogo, 650-0017, Japan

ARTICLE INFO

Article history:
Received 8 May 2009
Received in revised form 22 July 2009
Accepted 22 July 2009

Keywords:
Lung
Magnetic resonance (MR)
Lung cancer
Perfusion
Lung function

ABSTRACT

Purpose: The purpose of this study was to compare predictive capabilities for postoperative lung function in non-small cell lung cancer (NSCLC) patients of the state-of-the-art radiological methods including perfusion MRI, quantitative CT and SPECT/CT with that of anatomical method (i.e. qualitative CT) and traditional nuclear medicine methods such as planar imaging and SPECT.
Materials and methods: Perfusion MRI, CT, nuclear medicine study and measurements of $\%FEV_1$ before and after lung resection were performed for 229 NSCLC patients (125 men and 104 women). For perfusion MRI, postoperative $\%FEV_1$ ($po\%FEV_1$) was predicted from semi-quantitatively assessed blood volumes within total and resected lungs, for quantitative CT, it was predicted from the functional lung volumes within total and resected lungs, for qualitative CT, from the number of segments of total and resected lungs, and for nuclear medicine studies, from uptakes within total and resected lungs. All SPECTs were automatically co-registered with CTs for preparation of SPECT/CTs. Predicted $po\%FEV_1$s were then correlated with actual $po\%FEV_1$s, which were measured $\%FEV_1$s after operation. The limits of agreement were also evaluated.
Results: All predicted $po\%FEV_1$s showed good correlation with actual $po\%FEV_1$s ($0.83 \leq r \leq 0.88$, $p < 0.0001$). Perfusion MRI, quantitative CT and SPECT/CT demonstrated better correlation than other methods. The limits of agreement of perfusion MRI ($4.4 \pm 14.2\%$), quantitative CT ($4.7 \pm 14.2\%$) and SPECT/CT ($5.1 \pm 14.7\%$) were less than those of qualitative CT ($6.0 \pm 17.4\%$), planar imaging ($5.8 \pm 18.2\%$), and SPECT ($5.5 \pm 16.8\%$).
Conclusions: State-of-the-art radiological methods can predict postoperative lung function in NSCLC patients more accurately than traditional methods.

1. Introduction

Despite advances in radiation therapy and chemotherapy, surgery is currently considered the best curative option for stage I, II or IIIA non-small cell lung cancer (NSCLC). However, many potentially resectable tumors occur in individuals with abnormal pulmonary function usually due to chronic obstructive pulmonary disease (COPD) or interstitial lung disease (ILD), thus increasing operative risk. Clinicians are therefore frequently asked to evaluate the risks and feasibility of lung resection for patients with multiple co-morbidities and prediction of postoperative lung function [1,2].

Currently, a few guidelines proposed by the American College of Chest Physicians and/or algorithms recommended for prediction of postoperative lung function may be used to estimate the amount of functional lung tissue that would be lost with surgical resection in NSCLC patients with a preoperative forced expiratory volume in 1 s (FEV_1) or diffusing capacity for carbon monoxide (DL_{CO}) of less than 80% [1–7]. In these patients, radiological examinations including ventilation or perfusion scans, quantitatively assessed CT based on density-masked CT technique or qualitatively assessed CT based on anatomic estimation are considered to be useful for prediction of postoperative lung function [1,8–17].

As well as traditional or newly proposed nuclear medicine and CT methods, dynamic contrast-enhanced MR perfusion imaging

☆ This work was partially supported by grants from Philips Healthcare and Bayer Pharma.
* Corresponding author. Tel.: +81 78 382 6104; fax: +81 78 382 6129.
E-mail addresses: yoshiharuohno@aol.com, yosirad@kobe-u.ac.jp, yosirad@med.kobe-u.ac.jp (Y. Ohno).

0720-048X/$ – see front matter © 2009 Elsevier Ireland Ltd. All rights reserved.
doi:10.1016/j.ejrad.2009.07.024

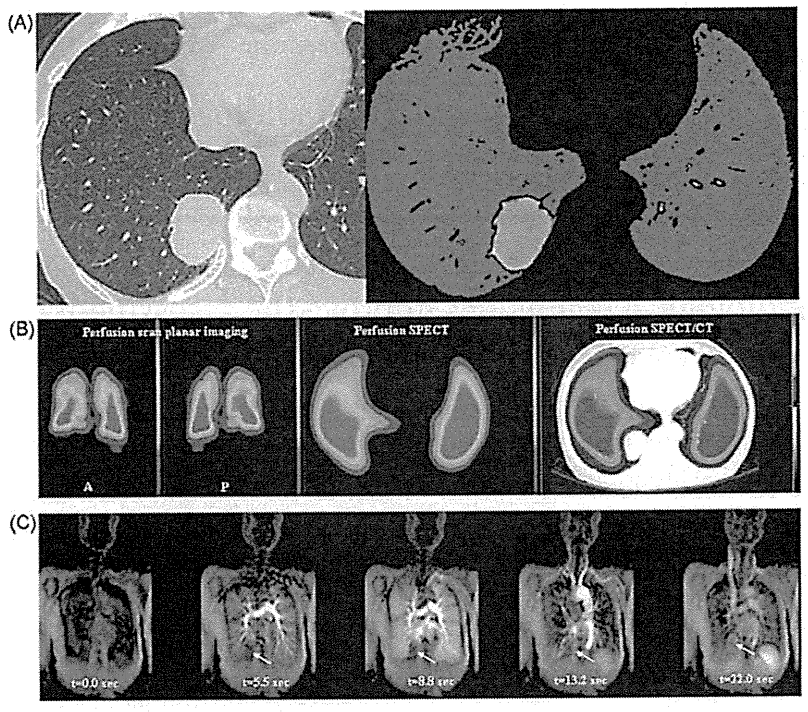

Fig. 1. 72-year-old female patient with squamous cell carcinoma in the right lower lobe. (A) L–R: thin-section CT and quantitatively assessed CT. Thin-section CT shows a mass in the right lower lobe, but no significant findings of emphysema. On quantitative CT, functional lung is shown in red, pulmonary emphysema in black, and lung cancer in white. There is slight emphysema in the right middle lobe and lingual segment. (B) L–R: anterior view of perfusion scintigraphy, posterior view of perfusion scintigraphy, SPECT and co-registered SPECT/CT. Perfusion scintigraphy shows reduced uptake of radioisotopes in the right lower lung field. Perfusion SPECT and co-registered SPECT/CT shows radioisotope deficiency due to lung cancer. In addition, the reduced uptakes in the middle lobe and lingual segment are thought to be due to emphysema. (C) L–R: $t = 0$, 5.5, 8.8, 13.2 and 22.0 s. t indicates the time after bolus injection of contrast media. Dynamic perfusion MR images demonstrate heterogeneously enhanced lung parenchyma due to emphysema and a non-enhanced area due to lung cancer (arrow) for 5.5 and 8.8 s. Enhancement of the lung cancer became gradually stronger during 13.2 and 22.0 s.

(perfusion MRI) has also been put forward as useful for the prediction of postoperative lung function in NSCLC patients [18–20]. Moreover, some investigators have suggested during the past decade that the use of single-photon emission tomography (SPECT), integrated SPECT/CT or fused SPECT image with CT (co-registered SPECT/CT) could result in improved predictive capability of postoperative lung function as compared with that of standard perfusion scan [21–24]. However, the number of patents enrolled in studies using these imaging techniques appears to be limited. No direct comparison of predictive capability among dynamic perfusion MRI, quantitative and qualitative CT, and nuclear medicine studies including perfusion scan, SPECT and co-registered SPECT/CT has been performed as yet.

For the study presented here, we hypothesized that dynamic perfusion MRI could predict postoperative lung function in NSCLC patients as accurately as quantitative CT and/or co-registered SPECT/CT, and had better potential for this purpose than qualitative CT, perfusion scan and perfusion SPECT. The purpose of this study was to directly and prospectively compare predictive capabilities for postoperative lung function in NSCLC patients of the state-of-the-art radiological methods including perfusion MRI, quantitatively assessed CT and SPECT/CT with that of anatomical method (i.e. qualitatively assessed CT) and traditional nuclear medicine methods such as planar imaging and SPECT.

2. Materials and methods

2.1. Subjects

Our institutional review board approved this study, and written informed consent was obtained from each subject prior to joining the study.

Between April 2006 and March 2008, 229 consecutive pathologically diagnosed lung cancer patients considered candidates for lung resection (125 men, 104 women, aged 53–82 years; mean age, 71 years) prospectively underwent preoperative contrast-enhanced MDCT, dynamic perfusion MRI and perfusion scan with SPECT examination (Fig. 1), and had their pre- and postoperative forced expiratory volume per 1 s (predicted percentage, $\%FEV_1$) measured. All preoperative radiological examinations were performed in random order and less than 2 weeks before or after MR examinations (mean, 4.5 days; range, 1–11 days).

Of the 229 patients, 113 had adenocarcinoma other than bronchioalveolar carcinoma (BAC), 57 had BAC, 38 squamous cell carcinoma, 15 large cell carcinoma, and 6 small cell carcinoma. Final diagnoses of all patients were confirmed by pathological diagnoses of resected specimens. Details of patient characteristics are shown in Table 1.

2.2. Physiological index and outcome measures

Pulmonary function testing was performed according to the American Thoracic Society standards [25,26] and with an automatic spirometer (System 9; Minato Ikagaku, Osaka, Japan). All subjects underwent pre- and postoperative pulmonary function testing. All preoperative pulmonary function spirometric tests were performed within 2 weeks prior to MR examination (mean, 6.4 days), and all postoperative pulmonary function spirometric tests performed within 24–48 weeks following surgery (mean, 32 weeks).

2.3. CT examination

All examinations were conducted with a multi-detector CT (MDCT) (Somatom Plus 4 Volume Zoom scanner; Siemens Med-

Table 1
Patient characteristics.

Age (years)	
Mean	71
Range	53–82
Sex (cases)	
Male	125
Female	104
Histological subtypes (cases)	
BAC	57
Adenocarcinoma except BAC	113
Squamous cell carcinoma	38
Large cell carcinoma	15
Small cell carcinoma	6
Operation (cases)	
Lobectomy	166
Bilobectomy	7
Pneumonectomy	14
Segmentectomy	28
Preoperative $\%FEV_1$ (%)	
Mean ± SD	80.2 ± 17.2
Range	45–120.0
Actual postoperative $\%FEV_1$ (%)	
Mean ± SD	69.4 ± 13.7
Range	37–99.8

BAC: bronchioalveolar carcinoma; $\%FEV_1$: forced expiratory volume per 1 s (predicted percentage); SD: standard deviation.

ical Solutions, Forchheim, Germany). The scans were performed from the lung apex to the diaphragm (4 mm × 1 mm collimation, 6:1 pitch, 300–350 field of view, 512 × 512 matrix, 140 kV, 110 effective mA s) and reconstructed as 2 mm-thick slices. Before the CT examination, patients practiced their breathing to produce full and consistent inspiration. CT was then performed during breath-holding at the end of full inspiration. Contrast media (Iopamiron 300; Bayer Pharma, Osaka, Japan) was administered to patients intravenously via an antecubital vein at 2–3 mL/s with a power injector (Auto Enhance; Nemoto Kyorindo, Tokyo, Japan) with an empiric scan delay of 20 s to delineate the boundaries between tumor and mediastinal structures.

2.4. Image and data analysis of CT

2.4.1. Quantitative prediction of postoperative lung function

For quantitative prediction of postoperative lung function from the functional lung volume, we used the assessment method described elsewhere [17,20]. After applying dual thresholds of −500 and −950 HU, total functional lung volume (TFLV) and regional functional lung volume (RFLV) of the lung or lobe to be resected were calculated by multiplying the area of each functionally relevant lung tissue by the slice thickness. The area of associated emphysema was excluded by the lower threshold value (−950 HU), and the areas of tumor-related air space loss, such as the tumor itself and postobstructive atelectasis or areas of non-tumor related air space loss, such as fibrosis and atelectasis due to previous tuberculosis, were also satisfactorily excluded during visual inspection of the functional lung volume map. Two chest radiologists with 7 and 18 years' experiences (K.M. and D.T., respectively) performed all quantitative assessments of functional lung volume by using commercially available software (Pulmo; Siemens Medical Solutions). The RFLV of a resected lung or lobe was determined for each slice as the sum of RFLVs calculated from regions of interest (ROIs) placed on the resected lobe or lung. Final values of TFLV and RFLV of the lung or lobe to be resected were determined as the averages of measurements by the two investigators.

Predicted postoperative $\%FEV_1$ evaluated by quantitative assessment of CT (quantitative CT) examination ($po\%FEV_{1\,Quantitative\,CT}$) was calculated from TFLV and RFLV with the following formula [17,20]:

$$po\%FEV_{1\,Quantitative\,CT} = \text{preoperative } \%FEV_1 \times \left(1 - \left[\frac{RFLV_{resected\ lung\ or\ lobe}}{TFLV}\right]\right). \quad (1)$$

2.4.2. Qualitative prediction of postoperative lung function

For qualitative prediction of postoperative lung function, a previously described method and frequently utilized in many surgical institutions [1,12,13,15] was used to obtain postoperative $\%FEV_1$ from preoperative pulmonary function testing data and information on the number of bronchopulmonary segments removed. To determine the number of bronchopulmonary segments removed, all studies were interpreted by two pulmonary surgeon with 18 and 26 years' experience (Y.M. and M.Y., respectively), and final assessments were made by consensus. The predicted postoperative $\%FEV_1$ obtained by qualitative CT examination ($po\%FEV_{1\,Qualitative\,CT}$) was then estimated with the following formula described in the past literatures [1,12,13,15]:

$$po\%FEV_{1\,Qualitative\,CT} = \text{preoperative } \%FEV_1 \times (1 - [S \times 0.0526]), \quad (2)$$

where S is the number of bronchopulmonary segments removed by lung resection. Each segment is considered to represent 1/19 of the lung function (1/19 = 0.0526). The lower lobes were assumed to have five pulmonary segments each, the right upper lobe three segments, the right middle lobe two segments, and the left upper lobe four segments [1,12,13,15].

2.5. Dynamic contrast-enhanced perfusion MRI

All MR studies were performed on two 1.5 T MR scanners (Gyroscan Intera and Achieva; Philips Healthcare, Best, The Netherlands) using a phased-array coil. Dynamic perfusion MRIs (TR 2.7 ms/TE 0.6 ms/flip angle 40°; 128 × 96 matrix, 256 × 192 reconstructed matrix; rectangular field of view, 450–530 mm × 315–371 mm) were acquired with a three-dimensional (3D) radio-frequency spoiled gradient-echo (GRE) sequence. An overlapping slice in the coronal plane in a left-to-right phase-encoded direction of a 3D-slab with a thickness of 100 mm and 10 partitions was used, resulting in an effective partition thickness of 10 mm and five-step real phase encoding in the slice direction. The temporal resolution was 1.1 s for each 3D data set. All patients were bolus administered with 3–5 mL of gadopentetate dimeglumine (Gd-DTPA, Magnevist; Bayer Pharma) via a cubital vein with an automatic infusion system (Sonic shot; Nemoto) at a rate of 3–5 mL/s, followed by 20 mL of saline solution at the same rate. The basic theory and application of dynamic perfusion MRI have been documented in previous reports [19,20]. After careful instruction, patients practiced the breath-holding technique before the MRI studies to reproduce precisely the same degree of inspiration for each scan series. On each scan, 20 images were obtained during a less than 25-s breath hold at end-inspiration. All 229 dynamic contrast-enhanced perfusion MRI examinations were completed successfully without any adverse effects being observed.

2.6. Image and data analysis of dynamic contrast-enhanced perfusion MRI

After administration of Gd-DTPA, signal intensity time course curves were generated by measuring the signal intensity in the ROIs delineated in the right upper, right middle, right lower, left upper, left middle and left lower lung fields of every slice (60 ROIs per patient) on the MRI scanner by using commercially available

software provided by Philips Medical Systems. Large vessels and pulmonary arteries were excluded from the ROIs. From each ROI, data were then transferred to and independently analyzed with a personal computer (DELL Precision; DELL, Tokyo, Japan) using Microsoft Excel 2003 software (Microsoft, Redmond, WA) by two chest radiologists with 7 and 15 years' experience (H.K. and Y.O., respectively).

In order to extract quantitative indexes, the signal intensity time course curves were fitted to a gamma variate function by using the following equation [5] described in the literature [19,20]:

$$S(t) = S_{peak} \times \left(\frac{e}{\alpha\beta}\right)^{\alpha} \times (t - T_a)^{\alpha} \times e^{(-[t-T_a]/\beta)} + S_0, \quad (3)$$

where t is the time and $S_{(t)}$ is the measured signal intensity as a function of time. S_0 and S_{peak} are the baseline and peak signal intensities, respectively. T_a is the arrival time of the contrast bolus, and α and β are fitting parameters of the gamma variate function. Because of the small dose of injected contrast agent, it was assumed that a linear relationship exists between first-pass MRI signal intensity and contrast medium concentration in the ROI.

From the gamma variate function, the apparent mean transit time was calculated as the first moment on the MRI signal intensity–time curve by means of the equation [6] also found in the literature [19,20]:

$$\text{Mean transit time (MTT)} = \frac{\int t \times (S_{(t)} - S_0)\,dt}{\int (S_{(t)} - S_0)\,dt}. \quad (4)$$

The regional pulmonary blood volume was calculated directly from the area of the MRI signal intensity time course curve for a given ROI. Using the central volume principle, regional blood flow in each ROI (Q_{ROI}) was determined by dividing pulmonary blood volume by mean transit time [19,20]. Q_{ROI} was then normalized to the integrated arterial input function from the main trunk of the pulmonary artery [19,20]. The approximate time for an ROI measurement was 1 min.

To determine the regional perfusion in a lung field on dynamic contrast-enhanced perfusion MRI for prediction of postoperative lung function, Q in an ROI evaluated by dynamic perfusion MRI (Q_{MR}) was calculated as follows:

$$Q_{MR}\ (\%) = \frac{\sum_{n=1}^{10} Q_{ROI(n)}}{\sum_{n=1}^{10} (Q_{RUL(n)} + Q_{RML(n)} + Q_{RLL(n)} + Q_{LUL(n)} + Q_{LML(n)} + Q_{LLL(n)})} \times 100, \quad (5)$$

where n is the slice number, $Q_{ROI(n)}$ the Q of the ROI, $Q_{RUL(n)}$ the Q of the right upper lung field, $Q_{RML(n)}$ the Q of the right middle lung field, $Q_{RLL(n)}$ the Q of the right lower lung field, $Q_{LUL(n)}$ the Q of the left upper lung field, $Q_{LML(n)}$ is the Q of the left middle lung field, and $Q_{LLL(n)}$ the Q of the left lower lung field, all on slice number n.

To evaluate the predictive capability for postoperative lung function, the postoperative %FEV_1 predicted by dynamic perfusion MRI (po%$FEV_{1\,MRI}$) was calculated as follows:

$$\text{po\%FEV}_{1\,MRI} = \frac{\text{preoperative \%FEV}_1 \times (100 - Q_{MR} \text{ of resected lung or lobe})}{100}. \quad (6)$$

The details of calculation of regional blood flow and po%$FEV_{1\,MRI}$ have been described elsewhere [19,20].

2.7. Perfusion scintigraphic examination

For standard perfusion scintigraphic examination, perfusion planar and SPECT data were obtained by means of the e-CAM SPECT system (Siemens Medical Solutions) equipped with a low-energy, high-resolution collimator and with the subject in the supine position. All perfusion SPECT examinations were performed without respiratory gating and by means of intravenous administration of 185 MBq of ^{99m}Tc-MAA.

All perfusion planar images were acquired with previously reported methods [14,16]. The matrix size of both ventilation and perfusion planar images was 128 × 128. Each perfusion SPECT was acquired with 60 projections over 360° by means of the step-and-shoot method. The integration time per image was 20 s, and the matrix size of both ventilation and perfusion SPECT images was 64 × 64. A total 38–49 transaxial sections of 6.4 mm thick covering the entire lungs were reconstructed by using a Butterworth prefilter (order no. 8, cut-off frequency 0.34 cycles/cm) and a ramp back projection filter. The lung contour of each subject was drawn

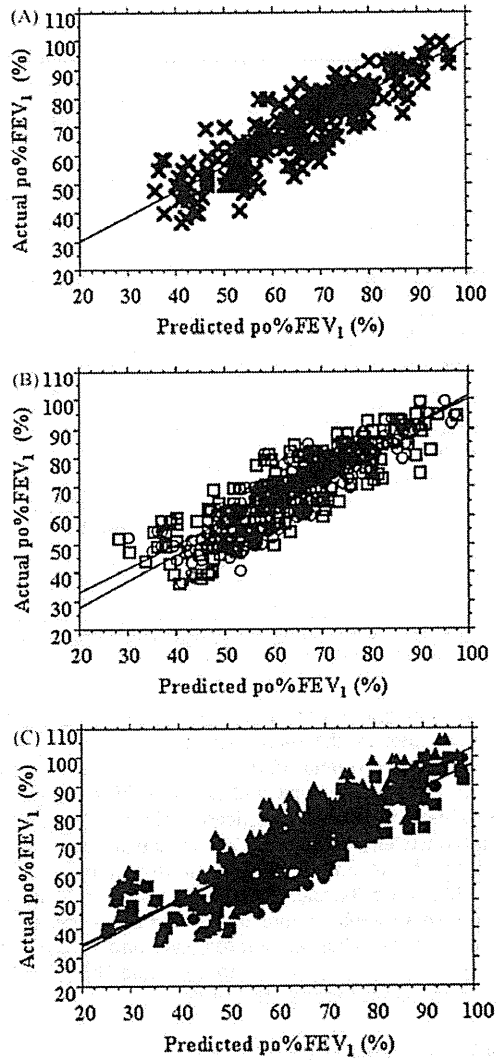

Fig. 2. Correlation between predicted po%FEV_1s ((×) dynamic perfusion MRI; (○) quantitative CT; (□) qualitative CT; (●) planar imaging; (■) SPECT; (▲) co-registered SPECT/CT) and corresponding actual po%FEV_1s. (A) po%FEV_1s predicted by dynamic perfusion MRI showed significant and good correlation with actual po%FEV_1s ($r = 0.88$, $p < 0.0001$). (B) po%FEV_1s predicted by quantitative CT ($r = 0.88$, $p < 0.0001$) and qualitative CT ($r = 0.85$, $p < 0.0001$) showed significant and good correlation with actual po%FEV_1s. (C) po%FEV_1s predicted by planar imaging ($r = 0.83$, $p < 0.0001$), SPECT ($r = 0.85$, $p < 0.0001$) and co-registered SPECT/CT ($r = 0.88$, $p < 0.0001$) showed significant and good correlation with actual po%FEV_1s.

Table 2
Mean difference and the limits of agreement of each method between actual and predicted postoperative lung functions.

	Mean difference (mean ± standard error)	Limits of agreement (%) (mean ± 2SD)
Quantitative CT	4.7 ± 0.4	4.7 ± 14.2
Qualitative CT	6.0 ± 0.5	6.0 ± 17.4
Planar imaging	5.8 ± 0.5	5.8 ± 18.2
SPECT	5.5 ± 0.5	5.5 ± 16.8
Co-registered SPECT/CT	5.1 ± 0.5	5.1 ± 14.7
Dynamic perfusion MRI	4.4 ± 0.5	4.4 ± 14.2

at a threshold of 15% of the maximum radioactivity of the lung. The energy window of Tc-99m was 140 keV ± 10%.

2.8. Automated co-registration of SPECT and CT images

All CT data, which were reformatted to a 256 × 256 matrix, were transferred to a personal computer, the FMV-900 (Fujitsu, Tokyo, Japan), and co-registered to SPECT data by using NEUROSTAT, which is a fully automated 3D registration software using a rigid body transformation technique [27,28]. This automatic registration algorithm has been in general use for co-registration for CT, magnetic resonance imaging (MRI) and nuclear medicine procedures such as SPECT and positron emission tomography (PET), and has been described in previous literatures [27,28]. Briefly, after SPECT slices had been re-sliced in accordance with the CT slices, the body contour was automatically found on SPECT and CT images with a simple gradient threshold technique. Fully automated co-registration was possible regardless of differences in slice range and thickness of the object between SPECT and CT scans. After segmentation of the body contour, the voxels inside the thorax were clustered into a set of connected components, and a rigid three-dimensional body transformation of SPECT images was performed to obtain the best matching images with CT. If apparent miss-registration was detected in the first fully automated procedure, the second automated co-registration could be applied after manual and gross matching of SPECT and CT images on three orthogonal section images. To visually distinguish CT from SPECT information on fusion images, CT images were displayed on a gray scale and SPECT images on a color scale. Image fusion process was completed within 1–2 min.

2.9. Image and data analysis of perfusion planar imaging, SPECT and co-registered SPECT/CT

For prediction of postoperative lung function by means of perfusion planar imaging, rectangular ROIs were drawn twice over the lobe or segment, which was later resected, and the whole

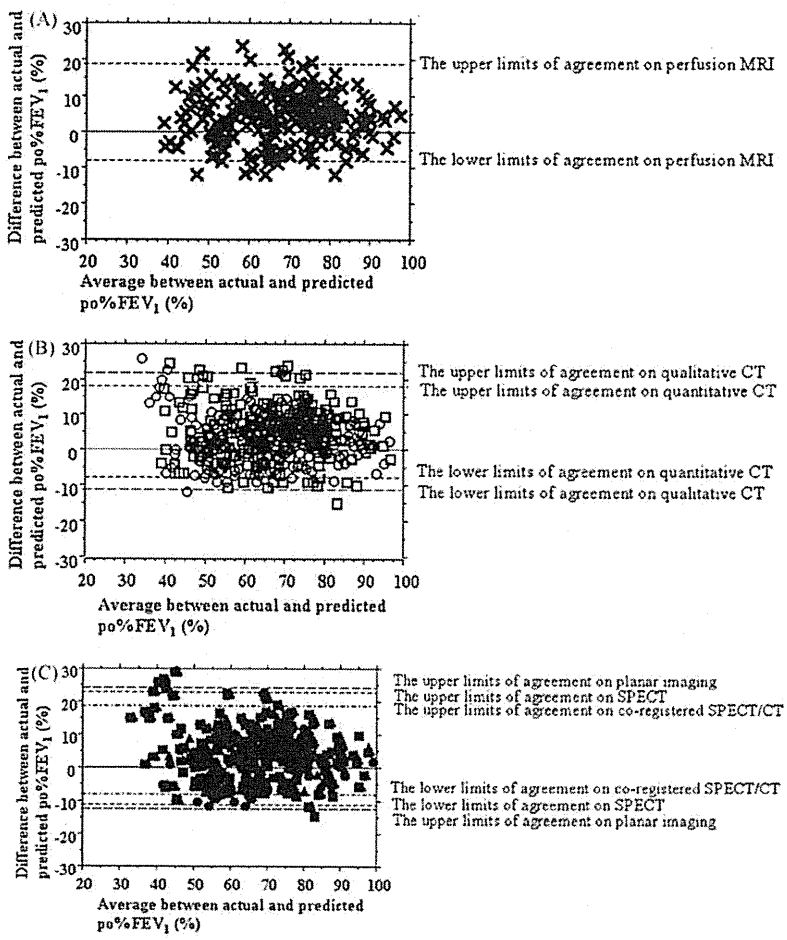

Fig. 3. Limits of agreement between predicted po%FEV_1s ((×) dynamic perfusion MRI; (○) quantitative CT; (□) qualitative CT; (●) planar imaging; (■) SPECT; (▲) co-registered SPECT/CT) and corresponding actual po%FEV_1s. (A) The limits of agreement for dynamic perfusion MRI were 4.4 ± 14.2%. (B) The limits of agreement for quantitative CT, and qualitative CT were 4.7 ± 14.2% and 6.0 ± 17.4%, respectively. (C) The respective limits of agreement for planar imaging, SPECT and co-registered SPECT/CT were 5.8 ± 18.2%, 5.5 ± 16.8% and 5.1 ± 14.7%.

lung in both the anterior and posterior images by two nuclear medicine physicians with 5 and 8 years' experiences (Y. Oni. and M.N., respectively), who also had more than 3 years' experience in chest radiology. Each time, both lungs were divided into five ROIs in the right upper, right middle, right lower, left upper, and left lower lobes. The summed radioactivity within the ROIs placed over the resected lobe and total lung activity were measured by both investigators, and averaged to determine the final values for each subject.

Predicted postoperative $\%FEV_1$ evaluated by perfusion planar imaging ($po\%FEV_{1\,Planar\,imaging}$) was then evaluated according to the following formula described in the past literatures [14,16]:

$$po\%FEV_{1\,Planar\,imaging} = \text{preoperative } \%FEV_1 \times \left(1 - \left[\frac{\text{radioactivity of ROIs placed over the resected lobe on anterior and posterior images}}{\text{total lung activity on anterior and posterior images}}\right]\right). \quad (7)$$

For prediction of postoperative lung function with the aid of SPECT and co-registered SPECT/CT using ^{99m}Tc-MAA, ROIs were placed over the lobe, which was later resected, and the total lungs by the same nuclear medicine physicians. All ROI measurements were performed on the same personal computer with the same software. The summed radioactivity within the ROIs placed over the resected lobe and total lung activity were measured, and averaged to determine the final values for each subject. The predicted postoperative lung function assessed in terms of $\%FEV_1$ determined by SPECT ($po\%FEV_{1\,SPECT}$) or co-registered SPECT/CT ($po\%FEV_{1\,Co\text{-}registered\,SPECT/CT}$) was estimated by using the following formula found in the literature [20,23,24]:

$$po\%FEV_{1\,SPECT} \text{ or } po\%FEV_{1\,Co\text{-}registered\,SPECT/CT} = \text{preoperative } \%FEV_1 \times \left(1 - \left[\frac{\text{summed radioactivity within ROIs placed over the resected lobe}}{\text{total lung activity}}\right]\right). \quad (8)$$

2.10. Statistical analysis

To determine the capability of each modality to predict postoperative lung function, the correlation and the limits of agreement between actual and each version of predicted $po\%FEV_1$ were statistically evaluated. The limits of agreement between actual and predicted $po\%FEV_1$ were analyzed by means of Bland–Altman analysis.

To evaluate the interobserver agreement of the different versions of predicted $po\%FEV_1$, the reproducibility coefficient of each was calculated by means of Bland–Altman analysis.

A p value less than 0.05 was considered to be significant for all statistical analyses. The basic theory and application of the limits of agreement have been documented in the literature [29].

3. Results

Correlation between every predicted $po\%FEV_1$ and the corresponding actual postoperative $\%FEV_1$ is shown in Fig. 2. All versions of $po\%FEV_1$ showed significantly good correlation with their corresponding actual $po\%FEV_1$ ($p < 0.0001$). $po\%FEV_{1\,Perfusion\,MRI}$ ($r = 0.88$, $r^2 = 0.77$), $po\%FEV_{1\,Quantitative\,CT}$ ($r = 0.88$, $r^2 = 0.77$) and $po\%FEV_{1\,Co\text{-}registered\,SPECT/CT}$ ($r = 0.88$, $r^2 = 0.77$) showed better correlation with actual $po\%FEV_1$ than did $po\%FEV_{1\,Qualitative\,CT}$ ($r = 0.85$, $r^2 = 0.72$), $po\%FEV_{1\,Planar\,imaging}$ ($r = 0.83$, $r^2 = 0.69$) and $po\%FEV_{1\,SPECT}$ ($r = 0.85$, $r^2 = 0.72$).

The limits of agreement between actual $po\%FEV_1$ and predicted $po\%FEV_1$ are shown in Table 2 and Fig. 3. For $po\%FEV_{1\,Perfusion\,MRI}$, the mean and standard error were 4.4% and 0.5%, and the limits of agreement ranged between −9.8% and 18.6%; for $po\%FEV_{1\,Quantitative\,CT}$, the corresponding values were 4.7% and 0.4%, and ranged between −9.5% and 18.9%; for $po\%FEV_{1\,Qualitative\,CT}$, 6.0% and 0.5% and between −11.4% and 23.4%; for $po\%FEV_{1\,Planar\,imaging}$, 5.8% and 0.5%, and between −12.4% and 24.0%; for $po\%FEV_{1\,SPECT}$, 5.5% and 0.5%, and between −11.3% and 22.3%, and for $po\%FEV_{1\,Co\text{-}registered\,SPECT/CT}$, 5.1% and 0.5% and between −9.6% and 19.8%.

The interobserver agreement for each of the $po\%FEV_1$s is shown in Fig. 4. Reproducibility coefficients (RCs) of dynamic perfusion MRI ($RC = 0.0 \pm 7.4\%$), quantitative CT ($RC = 0.0 \pm 7.0\%$) and co-registered SPECT ($RC = 0.0 \pm 7.6\%$) were smaller than those of planar imaging ($RC = 0.0 \pm 14.8\%$) and SPECT ($RC = 0.0 \pm 9.0\%$). In addition, RC of qualitative CT ($RC = 0.0 \pm 4.6\%$) was smaller than that of the other modalities.

4. Discussion

Our results demonstrated with a large prospective cohort of NSCLC patients that state-of-the-art radiological examinations comprising dynamic perfusion MRI, quantitatively assessed MDCT and co-registered SPECT/CT possessed better predictive capability for postoperative lung function than did qualitatively assessed MDCT and nuclear medicine perfusion studies such as planar imaging or SPECT. In addition, interobserver values for the state-of-the-art radiological examinations were almost the same and any variabilities were smaller than those for planar imaging and SPECT, while the reproducibility coefficient of qualitatively assessed MDCT was the smallest. With these state-of-the-art techniques, regional pulmonary function can be assessed on the basis of quantitatively assessed morphological changes and/or perfusion based information combined with anatomical information. To the best of our knowledge, ours is the first published study to directly compare the predictive capability and reproducibility of dynamic perfusion MRI with those of state-of-the-art and traditional methods based on MDCT and nuclear medicine techniques.

The correlation between actual and each of the predicted $po\%FEV_1$s in this study was significantly good. On the other hand, comparison of actual and predicted $po\%FEV_1$s showed that the correlations and the limits of agreement of dynamic perfusion MRI were superior to those of qualitative CT, planar imaging and SPECT, and almost identical to those of quantitative CT and co-registered SPECT/CT. In addition, the reproducibility coefficient of dynamic MRI was almost equal to that of quantitative CT and co-registered SPECT/CT, and smaller than that of planar imaging and SPECT. Because the limits of agreement and reproducibility coefficients of dynamic perfusion MRI as well as of quantitative CT and co-registered SPECT/CT can be considered small enough for clinical purposes, dynamic perfusion MRI can be substituted for qualitative CT and perfusion study assessed by planar imaging and SPECT, and merits consideration as being at least as useful as quantitative CT and co-registered SPECT/CT.

For the prediction of postoperative lung function by dynamic perfusion MRI, regional and total functional lung volumes were

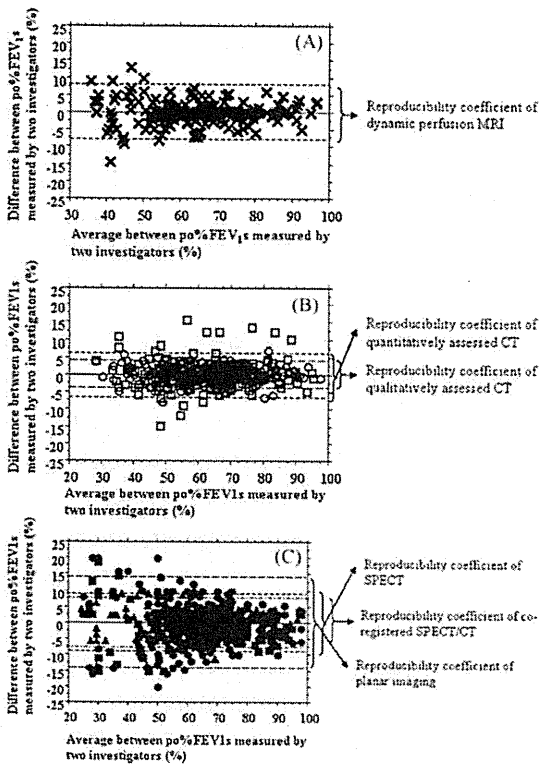

Fig. 4. Interobserver agreement between two investigators for predicted po%FEV_1 ((×) dynamic perfusion MRI; (○) quantitative CT; (□) qualitative CT; (●) planar imaging; (■) SPECT; (▲) co-registered SPECT/CT) by method. (A) The interobserver agreement assessed as reproducibility coefficients for dynamic perfusion MRI was 0.0 ± 7.4%. (B) The interobserver agreement assessed as reproducibility coefficients for quantitative CT was 0.0 ± 7.0%, and that for qualitative CT was 0.0 ± 4.6%. (C) The interobserver agreement assessed as reproducibility coefficients for planar imaging was 0.0 ± 14.8%, for SPECT it was 0.0 ± 9.0%, and for co-registered SPECT/CT it was 0.0 ± 7.6%.

assessed based on regional perfusion, similar to the procedure for perfusion scan assessed in terms of planar imaging, SPECT and co-registered SPECT/CT. Our results therefore suggest that dynamic perfusion MRI as well as co-registered SPECT/CT is superior to planar imaging or SPECT for assessment of regional functional lung volume. Previous studies have demonstrated that regional perfusion parameters semi-quantitatively or quantitatively assessed on dynamic perfusion MRI show good or excellent correlation with those assessed on perfusion scan [18–20]. The superior predictive capability of dynamic perfusion MRI and co-registered SPECT/CT for postoperative lung function is thought to be mainly due to the assessment of functional and anatomical information in co junction with a higher spatial resolution than that of planar imaging and SPECT. Currently, guidelines from the American College of Chest Physicians and/or certain algorithms suggest that anatomically based prediction and/or perfusion scan are useful for this purpose [1–7]. However, our findings indicate that dynamic perfusion MRI as well as other state-of-the-art radiological examinations such as quantitative CT and co-registered SPECT/CT can replace other methods for prediction of postoperative lung function, and play a complementary role to the aforementioned guidelines and/or algorithms for evidenced-based recommendations [1–7].

In routine clinical practice, many pulmonary surgeons predict postoperative lung function by using a simple calculation based on the number of resected and total bronchopulmonary segments, and claim this method provides a satisfactory estimation of operative risks [1–7], while the reproducibility coefficient of this method is reportedly smaller than that of all other radiological examinations used in our study. This is certainly true for low-risk candidates with good preoperative pulmonary function test results. In addition, our findings suggest that the reproducibility of ROI placement on radiological images by radiologists and/or nuclear medicine physicians is more difficult to achieve than that of surgical treatment and prediction by pulmonary surgeons. However, our study found that the correlation coefficient was lower and limits of agreement of the qualitative CT method were larger than those of the other modalities. These findings suggest that the greater over- or underestimation of postoperative %FEV_1 with this simple calculation than that resulting from the use of other methods may be due to the omission of evaluation of associated pulmonary emphysema, functional loss due to obstructive atelectasis and the non-functional lung area surrounding lung cancer, ventilation–perfusion mismatch due to invasion of pulmonary vasculatures by central lung cancer and/or hilar lymph node metastases, as well as of the differences in size among various segments. When considering pulmonary resection for high-risk candidates, state-of-the-art radiological methods including dynamic perfusion MRI even though perfusion SPECT may therefore help to more accurately predict postoperative %FEV_1 in NSCLC patients.

There are certain limitations to this study. First, while all dynamic perfusion MRI examinations were successfully completed without adverse effects, and regional perfusion could be fully calculated from signal intensity–time course curves, lung cancer patients with severe chronic obstructive pulmonary diseases needed to "shallow-breathe" during data acquisition, resulting in slight deterioration of the image quality. For lung cancer patients with poor pulmonary function, the resulting poor breath-holding capability may thus result in an underestimation of regional perfusion and regional pulmonary function. However, since dynamic perfusion MRI is a new technique for estimation of postoperative lung function, future advances leading to faster scanning time may make this technique more practical.

Second, lung resection can improve postoperative pulmonary function of patients with severe emphysema similar to that obtained with lung volume reduction surgery. The resultant beneficial effects on lung elastic recoil and chest wall mechanics make it difficult to accurately predict postoperative lung function [30,31]. It is therefore necessary for lung cancer patients with severe emphysema to have their cardiopulmonary reserve evaluated by exercise lung function tests before lung resection, so that the prediction of postoperative lung function on dynamic perfusion MRI or other radiologic methods may be even more accurate.

Third, the timing of determining the postoperative physiological index and outcome measurements ranged from 24 to 48 weeks, and were not assessed at a specific time. This affected the determination of actual postoperative lung function and our statistical comparison of predicted and actual postoperative lung function.

Fourth, although we used commercially available software for prediction of postoperative lung function on quantitatively assessed CT and all nuclear medicine examinations in this study, our proprietary software for calculation of regional perfusion on dynamic perfusion MRI is not commercially available. Moreover, several reports have specified proprietary software for quantitative assessment of regional perfusion parameters [19,20,32–38]. In this study, we could therefore not compare prediction errors of our software with those of other software for the same patients. We therefore recommend that further investigations be conducted in the near future to determine the real significance of our software for prediction of postoperative lung function.

Lastly, in our study we compared capabilities for prediction of postoperative lung function of dynamic perfusion MRI, quantitatively and qualitatively assessed CT and nuclear medicine examinations. However, we did not compare their capabilities for

prediction of other pulmonary functional parameters such as static lung volume and oxygen diffusing capacity, survival, quality of life and cost-effectiveness. Neither could we compare the predictive capability of dynamic perfusion MRI with that of other MR techniques such as oxygen-enhanced MR imaging, hyperpolarized noble gas MR imaging and non-contrast-enhanced perfusion MRI. A larger prospective comparative study therefore seems to be warranted to determine the real significance of dynamic perfusion MRI as a substitute for other radiological methods for prediction of postoperative lung function in lung cancer patients in routine clinical practice.

In conclusion, state-of-the-art radiological methods comprising dynamic perfusion MRI, qualitatively assessed thin-section MDCT and perfusion SPECT/CT, can predict postoperative lung function more accurately than traditional methods according to anatomically based predictions and perfusion scans or SPECT in NSCLC patients. Dynamic perfusion MRI as well as qualitatively assessed CT and perfusion SPECT/CT may thus be able to play a complementary role in the prediction of postoperative lung function in routine clinical practice.

Acknowledgements

The authors wish to thank Yoshiyuki Ohno, MPH, Professor Emeritus, Nagoya University (Department of Preventive Medicine, Graduate School of Medicine) for his advice for the statistical component of this study.

The authors also wish to thank Yoshikazu Kotani, M.D. (Division of Cardiovascular and Respiratory Medicine, Department of Internal Medicine, Kobe University Graduate School of Medicine) and Miyako Satouchi, M.D. (Department of Pulmonary Medicine, Hyogo Cancer Center) for their contributions to this study. This work was partially supported by grants from Philips Healthcare and Bayer Pharma.

References

[1] Pierce RJ, Copland JM, Sharpe K, Barter CE. Preoperative risk evaluation for lung cancer resection: predicted postoperative product as a predictor of surgical mortality. Am J Respir Crit Care Med 1994;150:947–55.
[2] Bolliger CT, Jordan P, Solèr M, et al. Exercise capacity as a predictor of postoperative complications in lung resection candidates. Am J Respir Crit Care Med 1995;151:1472–80.
[3] Wyser C, Stulz P, Soler M, et al. Prospective evaluation of an algorithm for the functional assessment of lung resection candidates. Am J Respir Crit Care Med 1999;159:1450–6.
[4] Beckles MA, Spiro SG, Colice GL, Rudd RM, American College of Chest Physicians. The physiologic evaluation of patients with lung cancer being considered for resectional surgery. Chest 2003;123:105S–14S.
[5] Mazzone PJ, Arroliga AC. Lung cancer: preoperative pulmonary evaluation of the lung resection candidate. Am J Med 2005;118:578–83.
[6] Myrianthefs P, Batistaki C. Preoperative pulmonary evaluation in patients scheduled for lung operations. J BUON 2007;12:163–71.
[7] Colice GL, Shafazand S, Griffin JP, Keenan R, Bolliger CT, American College of Chest Physicians. Physiologic evaluation of the patient with lung cancer being considered for resectional surgery: ACCP evidenced-based clinical practice guidelines (2nd edition). Chest 2007;132:161S–77S.
[8] Wernly JA, DeMeester TR, Kirchner PT, Myerowitz PD, Oxford DE, Golomb HM. Clinical value of quantitative ventilation–perfusion lung scans in the surgical management of bronchogenic carcinoma. J Thorac Cardiovasc Surg 1980;80:535–43.
[9] Ali MK, Mountain CF, Ewer MS, Johnston D, Haynie TP. Predicting loss of pulmonary function after pulmonary resection for bronchogenic carcinoma. Chest 1980;77:337–42.
[10] Bria WF, Kanarek DJ, Kazemi H. Prediction of postoperative pulmonary function following thoracic operations. Value of ventilation–perfusion scanning. J Thorac Cardiovasc Surg 1983;86:186–92.
[11] Markos J, Mullan BP, Hillman DR, et al. Preoperative assessment as a predictor of mortality and morbidity after lung resection. Am Rev Respir Dis 1989;139:902–10.
[12] Kearney DJ, Lee TH, Reilly JJ, DeCamp MM, Sugarbaker DJ. Assessment of operative risk in patients undergoing lung resection. Importance of predicted pulmonary function. Chest 1994;105:753–9.
[13] Zeiher BG, Gross TJ, Kern JA, Lanza LA, Peterson MW. Predicting postoperative pulmonary function in patients undergoing lung resection. Chest 1995;108:68–72.
[14] Giordano A, Calcagni ML, Meduri G, Valente S, Galli G. Perfusion lung scintigraphy for the prediction of postlobectomy residual pulmonary function. Chest 1997;111:1542–7.
[15] Beccaria M, Corsico A, Fulgoni P, et al. Lung cancer resection: the prediction of postsurgical outcomes should include long-term functional results. Chest 2001;120:37–42.
[16] Bolliger CT, Gückel C, Engel H, et al. Prediction of functional reserves after lung resection: comparison between quantitative computed tomography, scintigraphy, and anatomy. Respiration 2002;69:482–9.
[17] Wu MT, Pan HB, Chiang AA, et al. Prediction of postoperative lung function in patients with lung cancer: comparison of quantitative CT with perfusion scintigraphy. Am J Roentgenol 2002;178:667–72.
[18] Iwasawa T, Saito K, Ogawa N, Ishiwa N, Kurihara H. Prediction of postoperative pulmonary function using perfusion magnetic resonance imaging of the lung. J Magn Reson Imaging 2002;15:685–92.
[19] Ohno Y, Hatabu H, Higashino T, et al. Dynamic perfusion MRI versus perfusion scintigraphy: prediction of postoperative lung function in patients with lung cancer. Am J Roentgenol 2004;182:73–8.
[20] Ohno Y, Koyama H, Nogami M, et al. Postoperative lung function in lung cancer patients: comparative analysis of predictive capability of MRI, CT, and SPECT. Am J Roentgenol 2007;189:400–8.
[21] Imaeda T, Kanematsu M, Asada S, et al. Prediction of pulmonary function after resection of primary lung cancer. Utility of inhalation–perfusion SPECT imaging. Clin Nucl Med 1995;20:792–9.
[22] Piai DB, Quagliatto Jr R, Toro I, Cunha Neto C, Etchbehere E, Camargo E. The use of SPECT in preoperative assessment of patients with lung cancer. Eur Respir J 2004;24:258–62.
[23] Suga K, Kawakami Y, Zaki M, Yamashita T, Shimizu K, Matsunaga N. Clinical utility of co-registered respiratory-gated (99m)Tc-Technegas/MAA SPECT-CT images in the assessment of regional lung functional impairment in patients with lung cancer. Eur J Nucl Med Mol Imaging 2004;31:1280–90.
[24] Ohno Y, Koyama H, Takenaka D, et al. Coregistered ventilation and perfusion SPECT using krypton-81m and Tc-99m-labeled macroaggregated albumin with multislice CT utility for prediction of postoperative lung function in non-small cell lung cancer patients. Acad Radiol 2007;14:830–8.
[25] American Thoracic Society. Standardization of spirometry—1987 update. Am Rev Respir Dis 1987;136:1285–98.
[26] American Thoracic Society. Lung function testing: selection of reference values and interpretative strategies. Am Rev Respir Dis 1991;144:1202–18.
[27] Minoshima S, Berger KL, Lee KS, Mintun MA. An automated method for rotational correction and centering of three-dimensional functional brain images. J Nucl Med 1992;33:1579–85.
[28] Minoshima S, Frey KA, Koeppe RA, Foster NL, Kuhl DE. A diagnostic approach in Alzheimer's disease using three-dimensional stereotactic surface projections of fluorine-18-FDG PET. J Nucl Med 1995;36:1238–48.
[29] Bland JM, Altman DG. Statistical methods for assessing agreement between two methods of clinical measurement. Lancet 1986;1:307–10.
[30] Korst RJ, Ginsberg RJ, Ailawadi M, et al. Lobectomy improves ventilatory function in selected patients with severe COPD. Ann Thorac Surg 1998;66:898–902.
[31] Sinjan EA, Van Schil PE, Ortmanns P, Van den Brande F, Hendriks JM, Eyskens E. Improved ventilatory function after combined operation for pulmonary emphysema and lung cancer. Int Surg 1999;84:185–9.
[32] Hatabu H, Tadamura E, Levin DL, et al. Quantitative assessment of pulmonary perfusion with dynamic contrast-enhanced MRI. Magn Reson Med 1999;42:1033–8.
[33] Levin DL, Chen Q, Zhang M, Edelman RR, Hatabu H. Evaluation of regional pulmonary perfusion using ultrafast magnetic resonance imaging. Magn Reson Med 2001;46:166–71.
[34] Ohno Y, Hatabu H, Murase K, et al. Quantitative assessment of regional pulmonary perfusion in the entire lung using three-dimensional ultrafast dynamic contrast-enhanced magnetic resonance imaging: preliminary experience in 40 subjects. J Magn Reson Imaging 2004;20:353–65.
[35] Nikolaou K, Schoenberg SO, Brix G, et al. Quantification of pulmonary blood flow and volume in healthy volunteers by dynamic contrast-enhanced magnetic resonance imaging using a parallel imaging technique. Invest Radiol 2004;39:537–45.
[36] Risse F, Semmler W, Kauczor HU, Fink C. Dual-bolus approach to quantitative measurement of pulmonary perfusion by contrast-enhanced MRI. J Magn Reson Imaging 2006;24:1284–90.
[37] Ohno Y, Murase K, Higashino T, et al. Assessment of bolus injection protocol with appropriate concentration for quantitative assessment of pulmonary perfusion by dynamic contrast-enhanced MR imaging. J Magn Reson Imaging 2007;25:55–65.
[38] Ohno Y, Hatabu H, Murase K, et al. Primary pulmonary hypertension: 3D dynamic perfusion MRI for quantitative analysis of regional pulmonary perfusion. Am J Roentgenol 2007;188:48–56.